TECHNISCHE UNIVERSITÄT WIEN
Vienna University of Technology

DIPLOMARBEIT

Characterization of beam quality effects on film dosimeters in proton beam therapy

zur Erlangung des akademischen Grades

Diplom-Ingenieur

im Rahmen des Studiums

Technische Physik

eingereicht von

Paul Heyes
Matrikelnummer 01028121

ausgeführt am Atominstitut
der Fakultät für Physik der Technischen Universität Wien
in Zusammenarbeit mit der Universitätsklinik für Strahlentherapie der Medizinischen Universität Wien

Betreuung
Betreuer: Univ.Prof. Dipl.-Ing. Dr.techn. Dietmar Georg
Mitwirkung: Andreas Resch, PhD

Wien, 17.01.2020

(Unterschrift Verfasser/in) (Unterschrift Betreuer/in)

Acknowledgements

I would first like to express my gratitude to Prof. Dietmar Georg for his supervision of this thesis and granting the possibility of carrying out research at the Medical University of Vienna and MedAustron.

I am especially grateful for having Andreas Franz Resch as my (co-)supervisor, not only for his continuous support, constructive criticism and helpful discussions concerning the project, but also appropriately assuming the need for coffee and/or beer and motivating me to cycle to MedAustron (and thus sparking a general interest in travelling larger distances by bike).

Furthermore I would like to thank the rest of the office at the Medical University of Vienna, Hermann Fuchs, Barbara Knäusl, Gerd Heilemann and Natalia Kostiukhina, for the welcoming atmosphere and enjoyable chats over lunch and during coffee breaks.

I also want to express my gratitude to friends made at university making it a pleasant time, especially Clara Patek, Angelika Monetti and Vera Teufelhart, who shared all the highs and lows of tutarials and lab exercises with me.

Last but not least I would like to thank my parents, Kate and Chris, my sister Elizabeth, and my girlfriend Gabi for their unwavering support and encouragement, as well as putting up with me during the process of this thesis and studies in general.

Contents

Abstract

Purpose: While a commonly-used dosimeter in radiotherapy, the use of radiochromic films in particle therapy is limited due to their strong dependence on beam quality. In the case of protons, previous research has reported an under-response of EBT3 films of up to 20% around the Bragg-peak, which has largely been associated with the linear energy transfer (LET). The main focus of this work lies on the investigation of beam quality to quantify and correct for the under-response of EBT3 films. Since exact measurements are necessary, additionally film analysis is reviewed in terms of the analytical relation between optical density (OD) and dose, the time-dependence of calibrations, and different readout methods of the scanned film image, with the aims of mitigating systematic errors and reducing statistical uncertainties.

Methods: Measurements of single energy beams of 62.4, 148.2 and 252.7 MeV and spread-out bragg peaks (SOBPs) were performed at the treatment and research facility MedAustron (Wiener Neustadt, Austria) in a water phantom, using EBT3 radiochromic films and an ionization chamber (Roos chamber) as validation. These experiments were accompanied by Monte-Carlo simulations using GATE v8.0, in order to infer LET and spectral information. Corrections were derived by fitting the acquired relative effectiveness (RE) of the films to the dose averaged LET, and by optimizing a weighting function over the LET spectra at points of different RE.

Results: Performing the film readout using the single red channel displayed a measurement uncertainty ranging from 13% to 2.6% for doses of 0.25 to 2.5 Gy, compared to higher values using the dual or triple channel readout method. Between 0.5 and 2.5 Gy all examined calibration functions exhibited residuals below 2%. Calibrations with a seperation of approximately half a year showed deviations in the order of 10% around 0.5 Gy between each other. EBT3 films displayed an under-response of up to 30% at the Bragg peak and the modulated peak of the SOBPs at the lowest beam energies used. A functional relationship between relative effectiveness and fluence averaged LET could not be confirmed, while it was possible to describe the quenching as a function of the dose averaged LET of protons, within the confidence interval. Applying a parametrized arcus tangens as a function of dose averaged LET to the nominal dose, agreed within 6% with the smoothed

uncorrected film dose. Optimization of weights over the LET spectrum at different RE yielded a nonlinear dependence of the RE over the LET spectrum.

Conclusion: For the dose range examined, single channel readout of the red channel was found to yield the most accurate results. While differences in choice of calibration function were negligible, performing the film calibration within measurement session was shown to have a large effect on accuracy. The film quenching was found to be a nonlinear function of LET, and dose averaged LET of protons, while fluence averaging was found to be conceptually limited. A nonlinear function of dose averaged LET, a parametrized arcus tangens, yielded the most accurate and robust correction of the film dose under-response. The spectral correction was more susceptible to measurement and simulation inacurracies, compared to the averaged LET approaches. Due to the high measurement uncertainties associated with steep dose gradients, the presented corrections are only valid up to approximately R80 (depth at which the dose has decreased to 80% of the maximum) and the dose fall-off, for the single energy beams and SOBPs, respectively. For more exact corrections, film dosimetry needs to be improved in terms of accuracy and precision.

Chapter 1

Introduction

In radiation therapy, cancer treatment relies on ionization (quantified with absorbed dose) in tumor cells, favourably resulting in their destruction, while minimizing the harm done to surrounding healthy cells. Since its first proposal in the mid 20th century (Wilson [1946]), proton (and ion) beam therapy has evolved to become a widespread cancer treatment possibility. Its main advantage, in comparison to conventional radiotherapy, is allowing for a spatially more confined dose distribution. In contrast to photon therapy, charged particles display a maximal energy deposition at the end of their range, referred to as the Bragg peak, followed by a steep dose fall-off. Since the range, and consequently the position of the Bragg peak, are dependent on the initial energy of the proton or ion beam, the large proportion of the dose can be localised according to a given treatment case, while reducing the dose to critical tissue in the vicinity. Figure 1.1 shows the depth-dose distribution of a proton and photon beam in tissue, illustrating the difference between the two.

In clinical practice, beams of different energies are combined (e.g., applied in succession), resulting in a spread-out Bragg peak (SOBP), in order to cover the target volume in depth. The modulation of the beam energy is determined by the type of accelerator in use. Synchrotron accelerators allow active selection of energy, whereas cyclotrons usually only deliver high energy beams (≈200 to 250 MeV), for which the energy is reduced to the desired extent by inserting material into the beamline (energy degrader). In order to achieve lateral spread to cover the tumor, the beam is either scattered on a material (passive scattering), or deflected in a magnetic field (active scanning), as described by Kubiak [2014]. Dynamic dose delivery methods such as intensity modulated therapy (IMT) are increasingly applied. In IMT the intensity of multiple beamlets is varied individually, allowing precise modelling of the dose distribution to complex shaped targets.

An obvious necessity for both research and treatment validation are accurate dose measurements, the requirement for higher (spatial) accuracy increasing with more

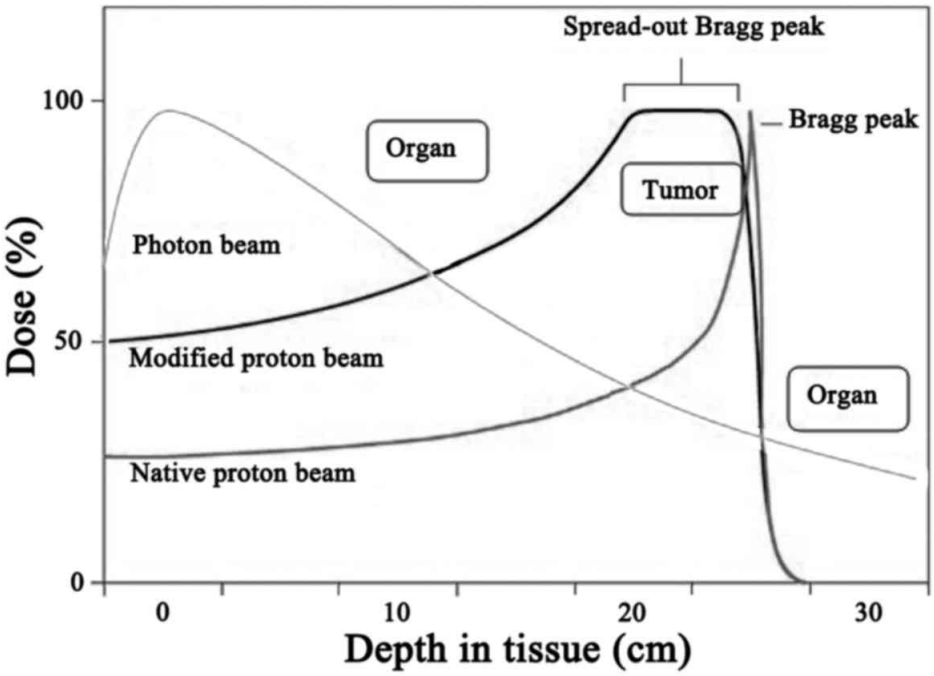

Figure 1.1: Dose deposition [%] over tissue depth [cm] for x-rays, protons and a modified proton beam (SOBP) in comparison. Image amended from Tian et al. [2018].

complex dose distributions and steep dose gradients. An ideal detector is tissue equivalent (has same material composition and density as the material of interest), has infinite resolution and yields reproducible results. A further requirement is that its physical interaction mechanisms and dependencies are well understood. In clinical practice ionization chambers (ICs) are widely used to measure the dose. However, due to their intrinsic design consisting of a gas-filled chamber (active volume), ICs are not tissue equivalent, perturbing the particle fluence. Further measurement constraints are given by the size of the detector and the resolution being limited to the active volume.

Passive detectors, such as thermoluminescent and optically stimulated dosimeters (TLDs and OSLDs), alanine or films, provide an alternative. They are of smaller or variable size, approximately tissue equivalent and allow measurements with higher spatial resolution. While these detectors are a commonplace dosimetry tool for photons and electrons, their use in proton or ion dosimetry is not trivial where they display an energy dependence. The main focus within this work lies on films. As previously documented (Kirby et al. [2010], Zhao and Das [2010], Castriconi et al. [2016] and Grilj and Brenner [2018] among others), GafChromic films exhibit an under-response around the Bragg peak region and distal fall-off of the spread-out Bragg peak (SOBP). This effect has been broadly associated with linear energy transfer (LET), hence the energy dependent response is often referred to as LET

quenching.

Aim of this project is to investigate the beam quality over clinically relevant beam energies and describe the film quenching effects, ideally finding a robust dose correction for GafChromic External Beam Therapy 3 (EBT3) films (International Specialty Products/Ashland Inc.), applicable over clinically relevant energies and doses. In previous literature different film quenching correction approaches can be found, ranging from linear (Anderson et al. [2019]) or polynomial (Perles et al. [2013]) functions of the dose averaged LET, to corrections dependent on the entire energy spectrum at a given depth (Fiorini et al. [2014]). Such corrections are investigated and their quality determined based on the results obtained within the breadth of this work.

Chapter 2

Physics of light ion beam therapy

2.1 Physical interactions of hadrons with matter

Hadrons interact via the Coulomb force with the atomic electrons and the nucleus. Further interactions with matter consist of nuclear reactions and Bremsstrahlung, as summarised in table 2.1.

Table 2.1: Interaction mechanisms of charged particles in matter.

Type	Target	Result
Inelastic Coulomb scattering	Atomic electrons	Energy loss of incident particle, ionisation electrons (delta-rays)
Elastic Coulomb scattering	Nucleus	Change of incident particle trajectory
Inelastic nuclear interactions	Nucleus	Removal of primary particle, secondary particles
Radiation losses (Bremsstrahlung)	Nucleus	Energy loss, change of incident particle trajectory, Bremsstrahlung

The energy loss of hadrons is governed by inelastic Coulomb scattering with atomic electrons, leading to excitation or ionisation of the atoms and negligible change in direction of the incident particle. This is the main contribution to the particles energy loss. The main effect of Coulomb scattering with the nucleus of the target is the deflection of the projectile. The energy loss these interactions makes up more than 1% of the total energy loss only for small particle energies in the

order of 10 keV and below (NIST [2017]). Inelastic nuclear reactions lead to the production of secondary particles such as protons, neutrons or heavier ions. While Bremsstrahlung may be an important factor for electrons, it is negligible in the clinically relevant energy range in light ion beam therapy, with energies yielding a range in water up to 40 cm. For proton beam therapy this corresponds to energies up to 250 MeV.

2.1.1 Energy loss rate

In radiotherapy an exact description of the energy loss of particles in matter, as a direct consequence of their interaction mechanisms, is of paramount importance. The energy loss per unit path length $\frac{dE}{dx}$, also referred to as linear stopping power S, is the sum of all contributions, i.e. losses due to collisions with atomic electrons $\left(\frac{dE}{dx}\right)_{coll}$ (electronic stopping power), with the nucleus $\left(\frac{dE}{dx}\right)_{nuc}$ (nuclear stopping power) and due to radiation $\left(\frac{dE}{dx}\right)_{rad}$ (Seltzer et al. [2011]):

$$S(E) = -\left(\frac{dE}{dx}\right) = -\left(\frac{dE}{dx}\right)_{coll} - \left(\frac{dE}{dx}\right)_{nuc} - \left(\frac{dE}{dx}\right)_{rad} ..., \tag{2.1}$$

where E is the mean energy loss and x is the path length. It is often expressed independently of the mass density ρ, by $\frac{S}{\rho}$, which is referred to as mass stopping power.

Closely related, but not identical to the stopping power, is the linear energy transfer (LET). It is defined as the amount of energy an ionizing particle transfers to the material being traversed (Seltzer et al. [2011]). While the total stopping power includes interactions with the nucleus and radiative effects, the LET is defined regarding only interactions leading to electronic excitations. Differentiation is made between restricted and unrestricted LET. Since in many cases only the energy transferred in the vicinity of the primary particle track is of interest, only secondary particles of energy smaller than a specified energy threshold Δ are taken into account. Hence, secondary particles with higher energies (or larger range) that would carry energy far from the primary particle track are neglected, resulting in the restricted LET_Δ. The unrestricted LET_∞ on the other hand, which includes all energy transfers, is numerically identical to the electronic stopping power (see section 2.1.1).

The definition of LET above applies to a single particle or a monoenergetic beam. Due to the statistical nature of a particle beam (see section 2.2), a whole range of values is encountered in most experimental settings. Hence, average LET values are commonly used to characterize a radiation field: *track* or *fluence* (Papiez and Battista [1994]) averaged LET_t and *dose* averaged LET_d, defined as

$$LET_t = \frac{\int S(E)\phi(E)dE}{\int \phi(E)dE} \tag{2.2}$$

and

$$LET_d = \frac{\int S(E)D(E)dE}{\int D(E)dE}, \tag{2.3}$$

where $D(E) = S(E)\phi(E)$ is the dose and $\phi(E)$ the fluence-distribution.

Electronic stopping power

Electronic stopping power describes the energy loss of incident ions due to inelastic Coulomb scattering between projectile and atomic electrons of the traversed material (leading to excitation or ionisation). A well established formula was originally proposed by Bethe [1930] and Bloch [1933] with further corrections added later:

$$-\frac{1}{\rho}\left(\frac{dE}{dx}\right)_{coll} = 4\pi N_A^2 r_e^2 m_e c^2 \frac{Z}{A}\frac{z^2}{\beta^2}\left[\ln\frac{2m_e c^2\gamma^2\beta^2}{I} - \beta^2 - \frac{\delta}{2} - \frac{C}{Z} + F\right], \tag{2.4}$$

commonly referred to as the *Bethe-Bloch equation*, where N_A is Avogadro's number, r_e is the classical electron radius, m_e is the electron rest mass, c is the speed of light in vacuum, Z and A are the atomic number and atomic mass of the material being traversed, z is the charge of the projectile, $\beta = \frac{v}{c}$ with v being the speed of the incident particle , $\gamma = \sqrt{1-\beta^2}$, I is the mean excitation potential of the traversed material, and δ and C are density and shell corrections respectively. F incorporates higher order corrections, including finite size, Mott-, Barkas- and Bloch-effect (Ahlen [1980]).

The Bethe-Bloch equation is dependent on both the projectile and the target. However, since $\frac{Z}{A} \approx const.$ for target materials with $Z > 1$, particles with the same charge and velocity have similar rates of mass stopping power in different materials, except in hydrogen. A slow decrease of energy loss with increasing Z remains though, due to the other material-dependent terms, in addition to the proportionality to the target material's mass density.

As the particle slows down along its trajectory, the stopping power increases, initially slowly. At very low energies, i.e. just before the particle comes to rest, the energy loss reaches a sharp maximum followed by a steep fall-off. When plotting the energy loss as a function of penetration depth, this maximum is referred to as the Bragg peak.

The Bethe-Bloch equation is valid for hadrons, not for electrons, since they have a different energy loss due to their quantum mechanical indistinguishability from the shell electrons of the traversed material. Additionally, Bremsstrahlung has a much larger influence due to their small weight. For very low projectile velocities, comparable to those of orbital electrons, equation 2.4 is no longer valid for hadrons either. In this region, energy losses can be described by the Lindhard-Scharff model. Between the two aforementioned models, the low energy Anderson-Ziegler model may

be used (as seen in figure 2.1).

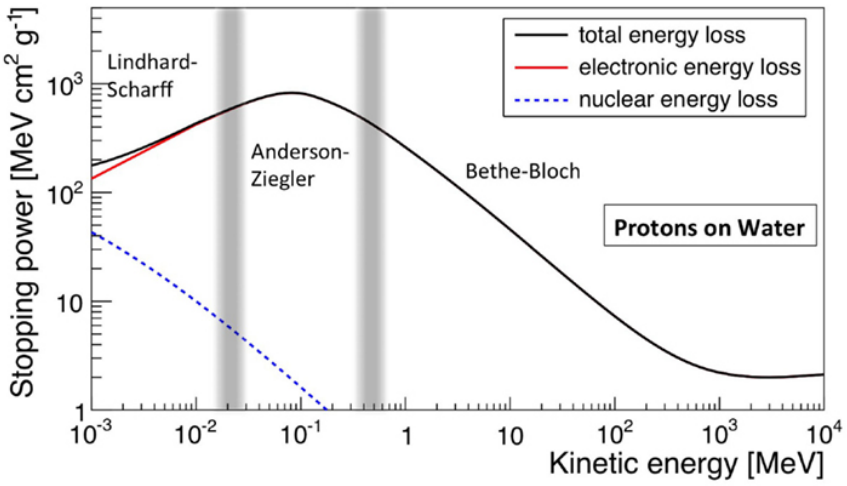

Figure 2.1: Stopping power $[\frac{MeV}{cm^2 g}]$ of protons in water, as a function of kinetic energy. Image amended from Kraan [2015]

Nuclear stopping power $\left(\frac{dE}{dx}\right)_{nuc}$

Elastic Coulomb interactions with atomic nuclei mainly cause a change in momentum direction of the projectile, resulting in the broadening of the beam. At very low energies however, the energy loss due to such interactions is no longer negligible, as can be seen in figure 2.1 for the case of protons in water. Widely used semi-empirical approaches obtain the nuclear stopping power by calculating the cross-section for elastic scattering of heavy charged particles by the screened Coulomb potential of the target atoms, followed by the transfer of energy to recoiling atoms in such collisions (Berger et al. [1993]).

Radiation losses (Bremsstrahlung) $\left(\frac{dE}{dx}\right)_{rad}$

To estimate the order of magnitude of Bremsstrahlung losses for protons, $\left(\frac{dE}{dx}\right)_{rad}$, the differential cross-section for bremsstrahlung of electrons valid for high energies ($> 1\,\text{GeV}$) is used (Tsai [1974]),

$$\frac{d\sigma}{dk} = 4\alpha \frac{e^2}{mc^2}\frac{1}{k}\left[\left(\frac{4}{3} - \frac{4}{3}y + y^2\right)\left(Z^2 F_{el} + Z F_{inel}\right) + \frac{1}{9}(1-y)(Z^2+Z)\right]. \quad (2.5)$$

Here $\frac{d\sigma}{dk}$ is the differential cross-section, dependent on the particle mass m, photon energy k, the fraction of photon to electron energy $y = \frac{k}{E}$, the atomic number Z and elastic and inelastic form factors F_{el} and F_{inel}. Integration of equation 2.5 yields

the mean energy loss, though only the dependencies on the incident particle are of interest here, i.e.

$$-\frac{1}{\rho}\left(\frac{dE}{dx}\right)_{rad} = N_A \int k\frac{d\sigma}{dk}dk \propto \frac{E}{m^2}. \tag{2.6}$$

The proportionality to m^{-2} is the defining factor, restricting radiative energy loss of the proton to an order of magnitude of 10^6 smaller than that of an electron with the same energy. Using stopping power data from the NIST database (NIST [2017]), the contribution of bremsstrahlung for protons of 250 MeV can thus be calculated to be around 10^{-7} of the total stopping power. Hence, energy loss due to radiation (i.e. Bremsstrahlung) is negligible for proton beams in the clinically relevant energy range.

Non-elastic nuclear interactions

Charged particles may also undergo non-elastic reactions with the atomic nucleus, in which the projectile and the target nucleus are transformed. These reactions have two main consequences. First, the projectile particles are depleted from the beam since the collision will change their nature. Secondly, this removal of particles is compensated by the liberation of secondary particles such as protons, neutrons or other ions.

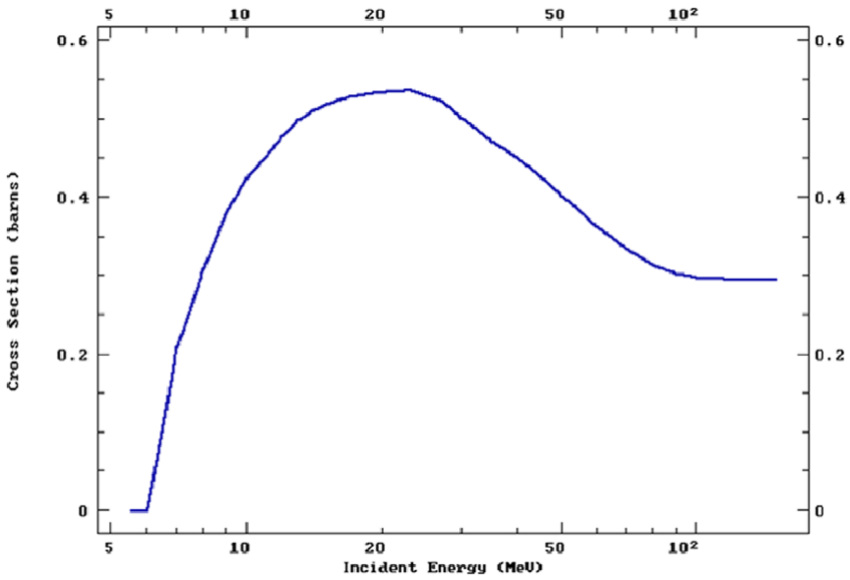

Figure 2.2: Total non-elastic nuclear cross-section of protons in oxygen over incident proton energy. Image source: Newhauser and Zhang [2015]

Nuclear reaction cross-sections are dependent on the atomic number of the nucleus

and the energy of the projectile. They show a threshold at low energies, which corresponds to the Coulomb barrier that a projectile must overcome in order to initiate a non-elastic nuclear reaction. Figure 2.2 shows the nuclear reaction cross-section for protons in oxygen versus incident proton energy. The threshold at around 6 MeV is followed by a maximum at 20 MeV, which are typical values for biologically relevant elements (Chadwick et al. [2011]).

In ion beam therapy fragmentation of both projectile and target is one of the more relevant processes to be studied, from which conclusions relevant to therapy can be drawn (Battistoni et al. [2016]). Secondaries emitted from the projectile fragments are forward peaked in terms of the beam direction due to the high velocity of the projectile, and travel with similar velocity as the projectiles. When considering ion beams, lower-Z fragments have an increased penetration depth compared to the projectiles, since the range (with same velocity) scales with $\frac{A}{Z^2}$ (Schardt et al. [2010]). The result is a low dose deposition behind the Bragg-peak, referred to as the fragmentation tail, which in turn is not seen in proton beams. Particles emitted from the target fragments are emitted almost isotropically and with lower energies, resulting in a low dose envelope around the beam (Kraft [2000] and Schardt et al. [2010]).

Concerning proton beams, secondary protons can make up a considerable amount of the absorbed dose, lead to a dose build-up effect (as can be seen in figure 2.3) due to their forward emission and higher stopping power, and affect the energy distribution of a beam (R.F. Laitano and Frisoni [1996], Paganetti [2002]). In Grassberger and Paganetti [2011], secondary proton dose contribution was determined to be up to about 10% in a 160 MeV beam, while alpha particles, deuterons and heavier ions only comprise as much as 1% of the delivered dose. In addition to their dose contribution, due to their lower energy, secondary particles display comparatively high LET-values. The LET_d of secondary protons is roughly a factor 10 higher than that of the primaries, larger factors applying for heavier reaction products. Consequently, not all secondary particles may simply be neglected when considering dose and LET, though these proportions do depend on the initial beam energy, with lower beam energies displaying smaller contributions from secondaries, as well as the depth, as shown in section 4.2.1.

2.2 Energy range relation

In general terms the range describes the depth a particle can travel through a medium, before it comes to rest at zero kinetic energy. Considering an entire beam rather than one particle, there are small differences in the energy loss of individual

particles (energy straggling), due to the statistical nature of their interactions with matter. Similarly, deflections from the original particle trajectory due to scattering result in variations in individual particle range. Hence, the range becomes a statistical quantity for a beam. It may be defined as the depth at which half of the protons incident on the absorber material have come to rest, or put in more practical terms considering the usual quantity of interest, the depth at which the dose has dropped to a certain dose threshold. Consequently different ranges are denoted by their percentage of peak dose, i.e. the range defined above is *R50*, while the range at 80% of the maximum dose would be *R80*.

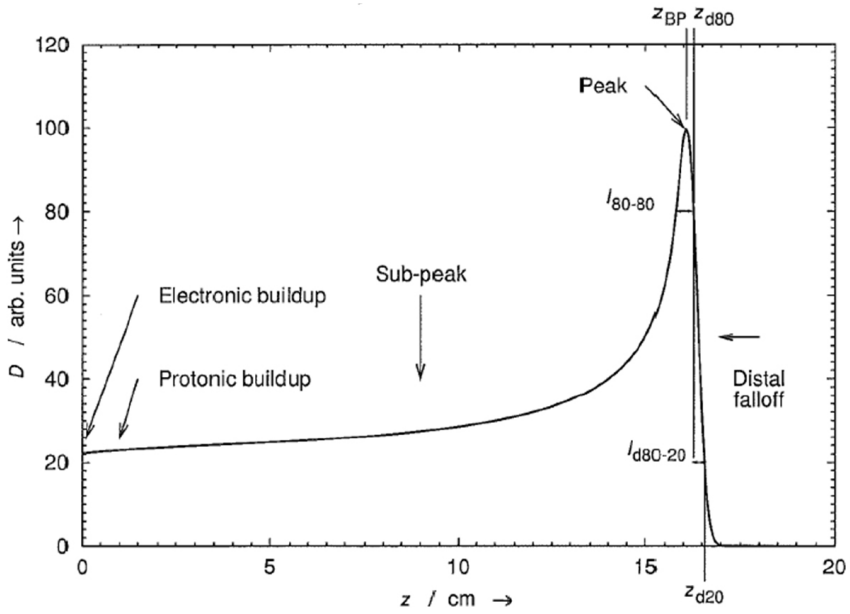

Figure 2.3: Dose-depth curve (Bragg curve) of a proton beam. Image source: Newhauser and Zhang [2015]

A good approximation of the range in cases where lateral scattering is negligible, can be made by integration of the reciprocal stopping power with respect to energy, i.e.

$$R(E) = \int_0^E \left(\frac{dE'}{dx}\right)^{-1} dE'. \tag{2.7}$$

This approximation assumes that the rate of energy loss is equal to the total stopping power at every point along the track, hence it is referred to as the *continuous-slowing-down approximation* (CSDA).

In charged particle therapy the thickness of materials is often expressed relative to water, yielding the water-equivalent thickness (WET), making range considerations easier when dealing with multiple materials being traversed. An approximate

calculation, given the ranges in water and arbitrary material, is (IAEA [2000])

$$t_w = t_m \frac{R_w}{R_m}, \tag{2.8}$$

where t_m is the 'true' material thickness, t_w is the WET, and R_w and R_m are the ranges in water and the material, respectively. Due to the energy dependence of the range (as seen in equation 2.7) the WET is consequently dependent on the energy too. However, for most materials of interest it is almost energy independent, for the clinically relevant energy range.

2.3 Dosimetry

Dose represents the mean amount of energy deposited in a unit volume of matter from ionizing radiation per unit mass, measured in Gray ($Gy = J/kg$). Measurements of this quantity can be performed with several types of dosimeters commonly applied in clinics and research, which may be roughly divided into two groups: Active dosimeters (mainly ionisation chambers) need a power supply but can display dose directly. On the contrary are passive dosimeters, functioning on the basis of thermoluminescent materials (TLDs) or optically stimulated luminescence (OSLDs), or radiochromic films.

2.3.1 Radiochromic films

A variety of films exist for radiotherapy applications, their designs differing depending on the dose range of interest. The emphasis of the external beam therapy (EBT) series is on patient dosimetry for low dose ranges of 0.2 to 10 Gy (EBT3) and 0.4 to 40 Gy (EBT-XD), while the MD and HD product lines are tailored to mid (<100 Gy) and high ranges (<1000 Gy), respectively. The active component of such films in general consists of monomer structures, which polymerize upon exposure to ionizing radiation, effectivey leading to the darkening of the film (Lewis [2010]). In the case of EBT3 films, used exclusively within this work, the active medium is lithium-10,12-pentacosadiynoate (LiPCDA) (Lewis and Chan [2016]). This is also true for the predecessor EBT2, the main difference between the two versions being structural changes, i.e., EBT2 is asymmetrical such that results are not independent of film orientation during irradiation, while EBT3 is symmetrical. Hence, most results of this older generation of EBT-film are still valid concerning EBT3 investigations (as reported by Reinhardt et al. [2012]).

EBT3 films consist of a 28 µm thick active layer, containing the active component, sandwiched between two 125 µm polyester substrates.

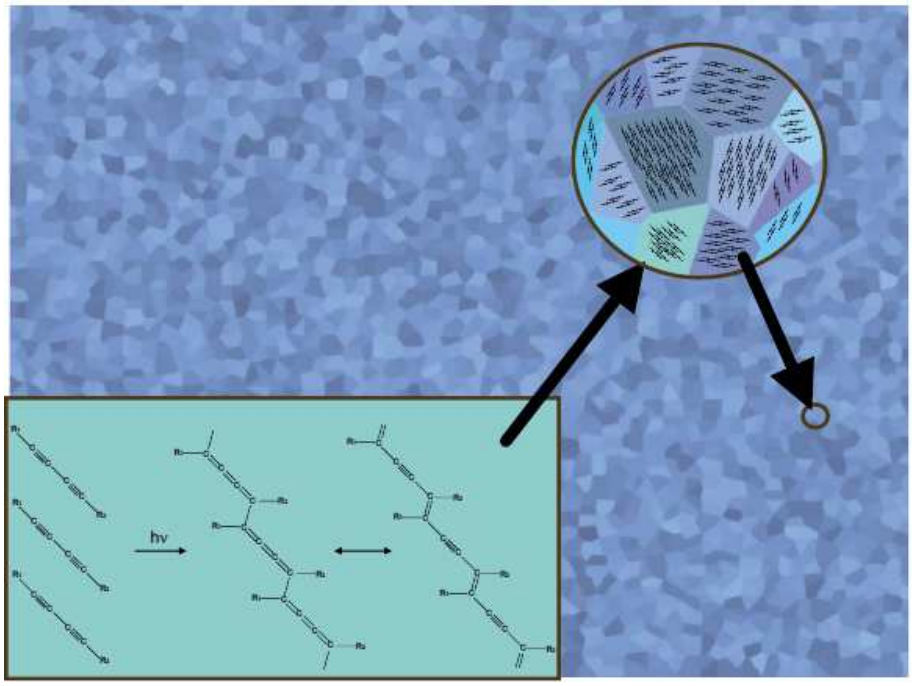

Figure 2.4: Illustration of polymerization process in the monomer crystals, induced by radiation. Image amended from Del Moral et al. [2009]

LiPCDA is a type of diacetylene, which, when in an ordered state, undergoes a 1,4 polymerization reaction upon exposure to ionizing radiation (Rink et al. [2008]), illustrated in figure 2.4. Initially diacetylene monomers polymerize to a butatrine structure polymer when exposed to ionizing radiation. Once the polymer chains propagate long enough, they reform into an acetylene structure via an intermediate, with a carbene (carbon atom with two unpaired electrons) at each end of the chain. Due to the increase in the formation of double bonds along the backbone of the polymers, caused by the polymerization, the absorbance of the polymer-monomer mixture increases, proportional to the delivered dose (Wegner [1972], Wegner [1977]).

In more detail, the polymerization process starts with ionizing radiation breaking a double bond, leading to the creation of a radical (molecule, atom or ion with an unpaired valence electron), which is very reactive. Electrons from double bonds are attracted to them, resulting in the breaking of the double bond and formation of a single bond with the radical. One electron from the former double bond is left alone, i.e. altogether a larger radical has been formed. This reaction propagates, forming a longer polymer chain. Termination of the polymerization process in the case of LiPCDA in Gafchromic films occurs as soon as the carbenes on either end of the chain reach an impurity or react with another carbene (i.e. another polymer). Impurities in this case are to be understood almost exclusively as large separations between polymer and adjacent monomer Rink et al. [2005b].

Mathematical description

The intensity I_0 of an incident beam of visible light traversing matter of concentration c and thickness d undergoes an exponential decrease, described by Beer-Lambert law

$$I = I_0 \exp\left(-\tilde{\epsilon} c d\right), \tag{2.9}$$

where $\tilde{\epsilon}$ is the attenuation coefficient.

The absorbance of films is usually expressed in terms of optical density (OD), defined as

$$OD = -\log_{10}\left(\frac{I}{I_0}\right) = \epsilon c d, \tag{2.10}$$

where I_0 and I are the intensities of the incident and emergent beam respectively. Equation 2.10 has significant consequences: The dependence of the OD on the thickness stresses the importance of addressing potential thickness variations in film dosimetry. Since the main change in concentration stems from polymerization, the OD is considered directly proportional to the number of polymerized monomers.

2.3.2 Dose response models for radiochromic films

Several different models have been used to describe the dose response of films. Previous literature has delivered justification for some models to be more robust than others (Del Moral et al. [2009], Martišíková and Jäkel [2010a]), by comparing the fit of these models to data from different sources. The selection of 3-parameter models introduced here is assumed to yield overall reliable results (since no contradicting information is availabe) and was not found to have been compared previously.

Bimolecular model

The bimolecular model was first found empirically by Schumann (Perles et al. [2013]) and later derived by Candler [1962] using the law of mass action, by modeling the chemical reaction response as an effect of the interaction of two atoms. Originally this was intended for the relationship between developed grains in photographic films and light exposure. Since the developed grains are comparable to activated monomers (which are proportional to the optical density) and light exposure is analogous to absorbed dose, the derivation may be applied to radiochromic films (Perles et al. [2013]). Thus the rate of activation of the monomers may be described as

$$\frac{dn}{dD} = k(1-n)^2 D^{(p-1)}, \tag{2.11}$$

where n is the fraction of activated monomers, $(1-n)$ is the fraction of available unactivated monomers, D is the dose, k is the reaction cross-section and p is a dimensionless parameter, determined experimentally. The first exponent in the equation implies that two molecules are required for the reaction. Expressing the fraction of molecules in terms of the OD the solution of equation 2.11 is

$$\frac{OD_{Bimol}}{OD'_{max} - OD_{Bimol}} = \left(\frac{D}{D_{1/2}}\right)^p, \tag{2.12}$$

where OD'_{max} is a constant proportional to the maximum OD, $D_{1/2} = (\frac{p}{k})^{\frac{1}{p}}$ is the absorbed dose at half of the maximum OD.

Gamma-distributed single-hit detector model

Among the models tested by Del Moral et al. [2009], for a dose range up to 5 Gy using different sets of experimental data, and Martišíková and Jäkel [2010a], for doses up to an order of 10^4 Gy, the gamma-distributed single-hit detector model was found to fit the OD-dose relation best in both cases. This model requires the monomers (active centers) to be hit by only one ionizing particle in order to polymerize (single hit detector). The active center cross sections are not assumed to be constant, since polymers may differ in size, but instead follow a gamma distribution (Del Moral et al. [2009]). The 3-parameter OD-dose relation is given by

$$OD_\gamma = OD_{max}\left(1 - \frac{a^b}{(a+D)^b}\right), \tag{2.13}$$

where OD_{max} is the maximum OD (defined as $OD_{max} := \lim_{D\to\infty} OD(D)$), and a and b are dimensionless parameters.

Empirical model

The supplier of EBT3 films introduced a fit-function with no apparent physical background (Micke et al. [2011]),

$$OD_{Emp} = -\log 10\left(\frac{a+bD}{c+D}\right), \tag{2.14}$$

with a, b and c being dimensionless parameters.

While these models account for the general dose dependency of films, they offer little insight into the mechanisms of the quenching effect occuring with higher LET. One possible explanation is offered by comparison to a similar effect in polymer gels. As is the case with films, the polymerization is dependent on the formation of free

radicals. In the case of high LET, the density of the free radical formation along a particle track becomes sufficiently high, such that a significant fraction can recombine (Gustavsson et al. [2004]). Alternatively, the possibility of local saturation has been hypothesised. Depending on the LET of an incident particle, a fraction of sites in the vicinity of the particle track are activated. Given a high enough LET, the local polymerization has saturated, and due to the spatial separation of the polymerization sites no further activation occurs (Jirasek and Duzenli [2002]).

2.4 Monte Carlo particle transport simulations

Monte Carlo (MC) methods describe the numerical solution of an underlying problem by random sampling over a large number of repititions. Classic applications are solving integrals or problems of probabilistic nature. Moreover, MC simulations represent a powerful tool for simulating particle transport through matter and retrieving information such as the dose distribution.

Prominent MC simulation software is the Geant4 toolkit, developed for high energy particle physics. In Geant4 primary and secondary particles are tracked through a user-specified geometry until zero kinetic energy, where the production of secondary particles can be prevented or multiplied by a threshold in terms of residual range (production cut). The interactions along the particle track are governed by the user-selected physics model, on which the simulation results are consequently strongly dependent. Due to the large set of physics models incorporated in Geant4, it is possible to sample particle interactions over a wide variety of species and a broad range of energy (Agostinelli et al. [2003]).

For medical applications, widely used software is GATE, a simulation platform based on the Geant4 toolkit, developed especially for numerical simulations in medical imaging and radiotherapy (Sarrut et al. [2014]). GATE offers many pre-defined routines for typical calculations in medical context, among them scoring routines for dose and LET.

Chapter 3

Materials and Methods

3.1 Design of experiments

3.1.1 Water vs RW3

Since in radiotherapy the depth is traditionally expressed relative to water, it is convenient to perform dose measurements directly in water, or in solid water equivalent material, for example in RW3 slab phantoms (PTW, Freiburg, Germany). Regarding film measurements, the main advantage of RW3 is its simplicity in use due to the rectangular design, allowing for the films to simply be stuck to the surface of the slab phantoms. A disadvantage of RW3 is that it is not exactly water equivalent. Previous measurements of the WET of RW3 performed at MedAustron differed in their results, posing an uncertainty for the simulations. What is more, activation of the RW3 plates could lead to longer measurement duration (as a safety precaution), which is not desireable considering the limited beam time. In addition to that, a tilt of the plates is not avoidable, diminishing the position accuracy.

Hence, it was preferential to perform the measurements in water, having the advantage of better range agreement with simulations (no WET needed), and the films being able to be extracted without touching the water, resulting in faster measurements. Regarding the placement of the films, the stepsize in depth is smaller in water, whereas it is limited by the smallest plate thickness of 1 mm when using RW3 plates, thus yielding greater versatility. Using films in water has been shown to be feasible, though it is recommended to perform a calibration in water (León-Marroquín et al. [2018]). Water may penetrate the active layer of the films, however this has been observed to be restricted to only a few mm from the edge of the film (approximately 4 mm after 24 h), which was further confirmed by brief in-house tests.

3.1.2 Film orientation

Regarding the film orientation with respect to the beam, approaches have been made by placing the films at a small angle to the beamline (for example Zhao and Das [2010]) or perpendicular to it (Kirby et al. [2010]). The former has the advantage that the entire dose profile can be acquired in one single measurement. However, the statistical uncertainty is large, due to a small surface averaged over per depth, which is especially dramatic when considering possible thickness variations of the film. In order to cover a large range, such a measurement setup requires large films, making the readout more prone to scanner artefacts. Additionally particles may travel within the film causing distorted results, dependent on the film angle, as is the case in Zhao and Das [2010]. Placing the films perpendicular to the beam allows for a readout of a large area of the flim, while avoiding scanner artefacts due to reducing the film size used. Since this leads to a more trustworthy result at given depths, this was the method of choice within this work.

3.1.3 Beam arrangement

Measurements of $7 \times 7\,\mathrm{cm}^2$ proton beams with 2 mm spot spacing were performed, of both single energy beams and SOBPs. Concerning the single energy beams, three beams of 62.4, 148.2 and 252.7 MeV were chosen, covering the energy range of clinically relevant beams.

Multiple beams are superimposed in order to achieve a spread-out Bragg peak. The weighting of the individual beams for a SOBP with given dose in the plateau was calculated using MC simulated dose distributions of the individual pencil beams (PBs). For each PB j the dose in voxel i was stored in a dose matrix $D_{i,j}$. The cost function χ^2 describes the squared difference between superimposed dose of beam with weight w_j and the planned dose $D_{planned,i}$ over the voxels of interest, i.e. voxels in the set P. The weight w_j of each beam was calculated by minimzing the cost function

$$\chi^2 = \sum_{i \in P} \left(\sum_j (D_{i,j} w_j) - D_{planned,i} \right)^2 . \tag{3.1}$$

The SOBPs were planned such, that they would deposit 1 Gy from 30 to 35 mm in depth. Beam $b1$ was composed of the lowest energies of 62.4, 63.5, 64.5, 65.5, 66.5 and 67.5 MeV, displaying the highest LET-values, while $b2$ and $b3$ had an additional 252.7 MeV beam contribution, associated with a lower LET. The difference between the latter two SOBPs is given by the different relative contribution of the individual beams. For $b2$ half of the protons were delivered by the low energy beams, the other

half by the 252.7 MeV beam. In the case of $b3$ half of the dose was delivered each by the low energy beams and the 252.7 MeV beam, respectively.

3.2 Experimental setup

3.2.1 Measurement setup

Dose measurements of proton beams in water were carried out at MedAustron, using a remotely controlled MP3-PL water phantom tank (PTW, Freiburg) with a spatial precision of 0.1 mm. Measurements done with a Roos Ionization Chamber (PTW, Freiburg) served as reliable reference data. Consequently, the EBT3 film measurements were set up to best mimic the IC. The same Trufix holder (PTW, Freiburg, Germany) is used as for the Roos chamber in order to enable identical positioning. EBT3 film sheets were cut into $2.5 \times 3.5\,\mathrm{cm}^2$ rectangles. Stacks of 3 to 6 of these rectangular films were fixed in the holder (as seen in figure 3.1a), clamped between a slab of plastic fitted in the holder and a RW3 plate. Due to this plate, and the multitude of films, corrections must be applied in order for the centre of an active layer of a film to be positioned at the desired water equivalent depth. These corrections were taken into account regarding the relationship between the position of the film active layer and the Roos active area (illustrated in figure 3.1b):

$$\begin{aligned} x_n = x_{roos} + wet_{roos-window} \\ -d_{roos} + d_{plate} \\ +Nd_{film} - (n - \frac{1}{2})wet_{film} \\ +d_{RW3} - wet_{RW3}. \end{aligned} \tag{3.2}$$

The occuring variables are shown in figure 3.1b, $wet_{variable}$ denotes the associated water equivalent thickness, n is the film index in the stack (1 denoting the film at smallest depth) and N is the total number of films in the stack.

3.2.2 Depth-dose measurements

Measurements of single energy proton beams of 62.4, 148.2 and 252.7 MeV, were conducted at a total of roughly 100 points in depth with the IC, and 250 points using EBT3 films. Based on the simulated depth-dose distribution, the positions were chosen such, that more data around the Bragg peak and distall fall-off would be available, compared to the plateau, since the LET quenching is largest near the end of range. For all beam energies some films were measured at reference conditions, i.e., positions close to entrance point of the beam in the water tank,

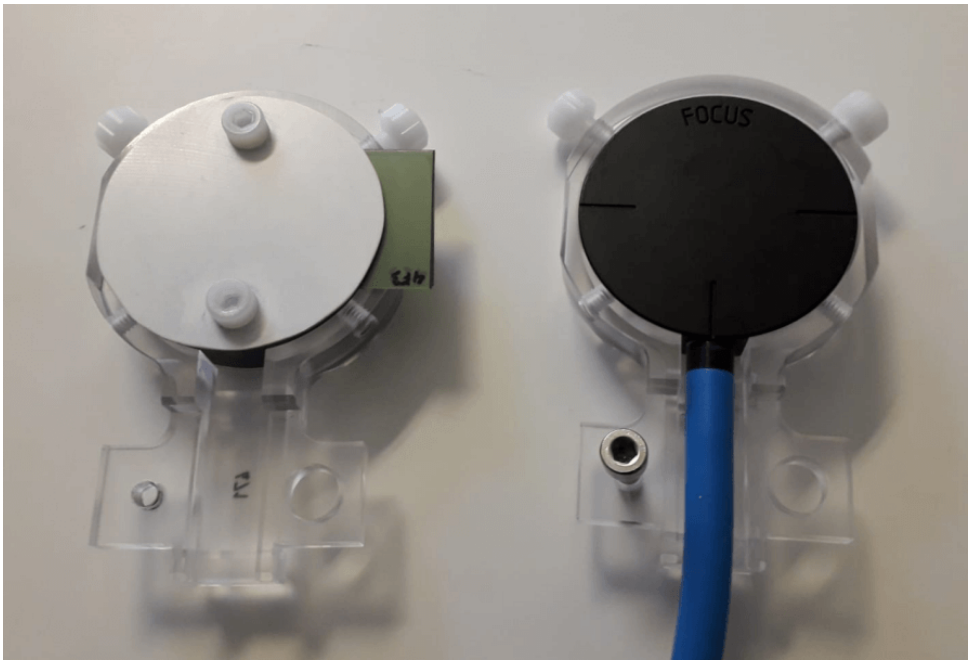

(a)

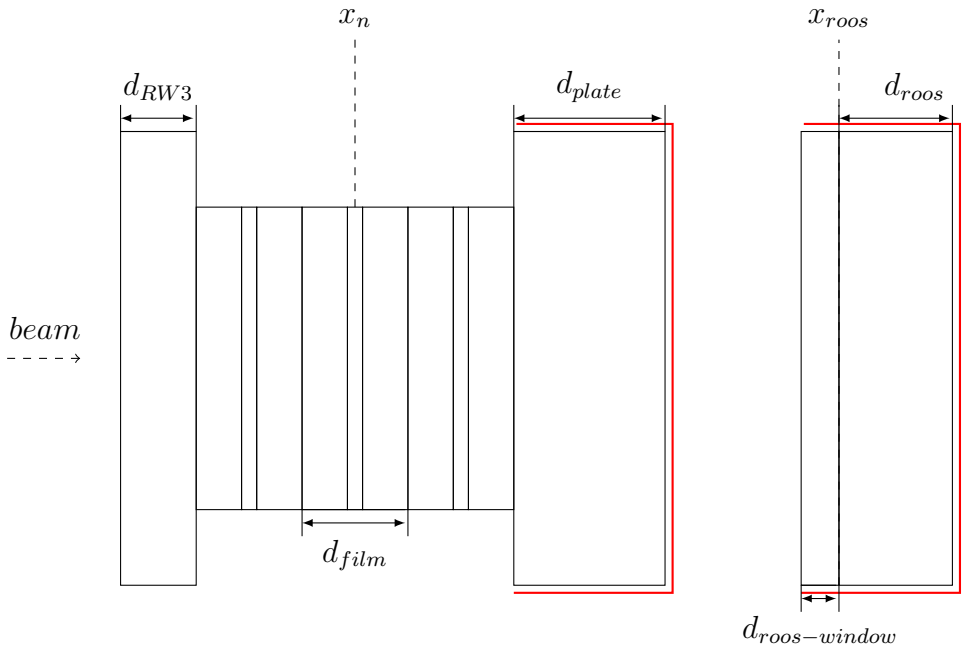

(b)

Figure 3.1: (a) Films (left) and Roos chamber (right) fixed in the Trufix holder. (b) Schematic illustration of films (left) and Roos chamber (right) in the Trufix holder (indicated in red). Dimensions not true to scale.

at which no under-response of the films is expected Martišíková and Jäkel [2010b]. For the beams measured here, these reference conditions were chosen at 1.4 cm (for the 62.4 MeV beam) and 2.0 cm (other beams). For the low energy beam this corresponds to an LET_d of roughly 1.64 keV/µm, while the 2 cm reference depth yields LET_d values of 0.93 and 0.84 keV/µm for the 148.2 and 252.7 MeV beams, respectively. Comprehensive measurements spanning over the entire Bragg peak were also sought after. Stacks of multiple films were used, with 3 films per stack for the plateau-measurements, and 6 films per stack in the peak region. The active layers of films within a stack were separated by one film thickness, limiting the resolution possible per stack. For example, in the case of the 62.4 MeV beam, this resolution amounts to about 40% of the Bragg peak width (proximal-80%-to-distal-80% peak width). In order to maintain sufficient resolution, the stacks of multiple films were positioned such that the individual film measurement positions would overlap those of other stacks in consequent irradiations.

Using the LET_d obtained in the MC simulations, depths of similar LET_d in beams of different energies were identified. Film positions were also chosen in order to retrieve film dose measurements of these points.

The three SOBPs were measured with the Roos chamber and EBT3 films over the modulated peak and around the distal falloff, between depths of 3.0 and 3.6 cm, at 10 points with the Roos chamber and 24 points per beam with the films. Stacks of 6 films were used, the positions of the films from different stacks overlapping analogous to the case for the single energy beams.

Measurements within this work were performed in the course of two seperate sessions, using films from the same batch. Calibration measurements of the films in water were performed at a depth of 2 cm in a 179.2 MeV proton beam at doses of 0.25, 0.5, 1.0, 1.25, 1.5, 2.0 and 2.5 Gy. However, such a calibration was only done during one of the measurement sessions, since it is common practice to perform a calibration only every now and then.

3.3 MC Simulations

Simulations of proton beams in water were performed using GATE v8.0 in combination with Geant4.10.3.p01, in order to retrieve dose deposition and LET. The physics list QBBC was used, which makes use of a combination of the binary and bertini cascade model for optimal results over a large energy range (Ivantchenko et al. [2012]). For modeling electromagnetic interactions standard option 4 (EMZ) was chosen (i.e., QBBC_EMZ). A specific beam model (Elia [2019]) was applied for the irradiation rooms at MedAustron. The maximum step size was set to 10 µm, the

production cuts for e^+, e^- and γ were set to 10 m. The mean excitation potential in water was 78 eV. The resolution in depth was set to 0.1 mm, equivalent to the assumed experimental measurement uncertainty.

The dose and averaged LET were scored using the GATE routines *GateDoseActor* and *GateLETActor*, respectively. Spectral information was retrieved via the *EnergySpectrumActor*.

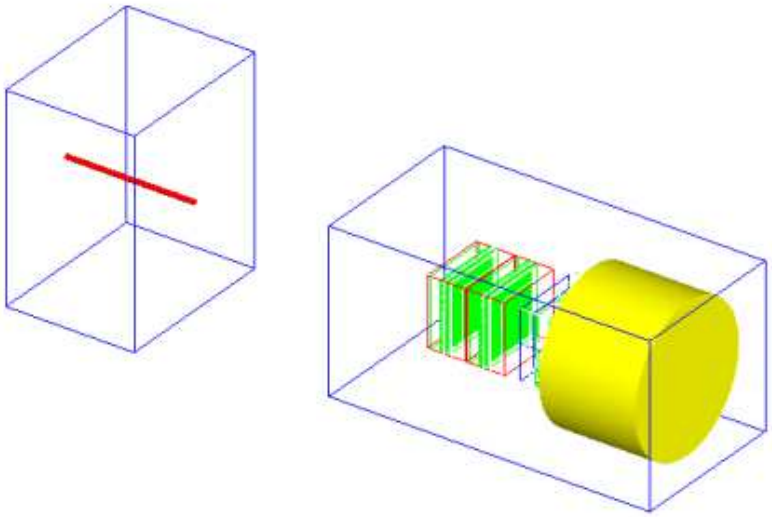

Figure 3.2: Illustration of geometry: The beams trajectory runs from the nozzle (block on the right) towards the water phantom (blue, to the left), in which the relevant quantities are captured in the Roos-chamber equivalent active area (red).

3.3.1 Single energy beams

MC simulations of 62.4, 148.2 and 252.7 MeV proton beams, in a water phantom were used to obtain the dose and LET_d of particles of interest. These physical quantities were evaluated in a cylindrical volume of 7.8 mm radius, with the rotational axis parallel to beam direction, as seen in figure 3.2, in order to mimic the active area of the Roos chamber used in the experiments. Different particle filters were incorporated to track the dose and LET_d of all particles, only protons, as well as primary and secondary protons seperately.

The number of primary events and production cut for protons varied with the simulations. General dose and LET investigations were performed prior to the measurements, as seen in section 4.2.1. Here the behaviour of dose and LET_d over depth, not only of the protons but also heavier particles, were of interest. Considering the low contribution of heavier particles, 10^8 primaries were simulated to

reduce the noise. The production cut for secondary protons was set to 500 µm, which corresponds to an energy of 6 MeV or an LET of roughly 6.85 keV/µm.

For all simulations used for comparison with the film measurements, 10^7 primary events were simulated with a production cut for protons of 5 µm. Such a low production threshold for protons was chosen to enable production of low energy protons, down to roughly 0.3 MeV, corresponding to an LET of approximately 50 keV/µm (obtained from the PSTAR-database, NIST [2017]). Additionally the mean energy and energy spread were altered for each beam, such that the simulated dose best fit the IC measurements. The final values are given in table 3.1.

Table 3.1: Mean energy and energy spread used in MC simulations.

Beam [MeV]	Mean energy [MeV]	Energy spread [MeV]	ΔE [%]
62.4	62.15	0.22	0.35
148.2	147.41	0.07	0.05
252.7	251.04	0.19	0.08

3.3.2 Spread-out Bragg peaks

In contrast to the single energy beams, for which an array of pencil beams, i.e., the entire beamfield, was simulated, a less calculation time intensive approach was chosen for the SOBPs. Here, a single pencil beam per energy comprising the SOBP was simulated, and the dose at given depth laterally integrated over the area of the desired beamfield (in this case up to a radius of $r = \frac{7cm}{\sqrt{\pi}}$, corresponding to the $7 \times 7\,\mathrm{cm}^2$ beam), making use of the reciprocity theorem. The simulated dose of the SOBPs was normalized to the five IC measurements in the plateau of the SOBPs, to account for day to day and seasonal fluctuations of the absolute dose. The simulation parameters for the SOBP simulations were not altered compared to the single beam simulations, including the number of primary events. As a consequence the single pencil beam simulations of the SOBPs display a higher resolution, since more of the primaries reach the detector.

3.3.3 LET spectra

Since GATE tracks all individual events within the simulation confinements, this was utilised to store all individual energy depositions and associated LET-values within volumes of 0.1 mm thickness at various depths (predominantly corresponding to film measurement positions) in the water phantom. In GATE, these were scored using the *EnergySpectrumActor*. The energy of each particle track is stored as the mean

of the particle energies at the *PreStep* and *PostStep* positions. The deposited energy is calculated via the *GetTotalEnergyDeposit()* method, which yields the energy transferred to the medium within the step. Likewise the LET is retrieved from the *GetElectronicDEDX()* method. This allows to score a histogram of the deposited energy differential in particle (kinetic) energy or LET.

Such energy and LET spectra were calculated for multiple depths in water, spanning over the entire depth investigated with the films. For the single energy beams, the resolution in depth was increased with depth, such that more data around the Bragg peak and fall-off would be available, since the distribution varies strongly with depth in this region. Regarding the SOBPs, the positions at which the spectra were obtained were evenly spaced out over the investigated area (i.e. the modulated peak and distal fall-off).

3.4 Film analysis

Films were scanned 36 h before and after irradiation, using an Epson Expression 10000 XL flatbed scanner (Epson, Suwa). The latter time window should allow for post-irraddiation darkening effects to take place, which may have a non-negligible effect on the results up to 24 h after irradiation (Butson et al. [2003], Rink et al. [2005a], Khachonkham et al. [2018]). The films were placed in the centre of the scanner to mitigate effects from the scan field non-uniformity (Paelinck et al. [2006]) and care was taken to warm up the scanner before each scan in order to reduce heat effects (Lynch et al. [2006]). Additionally a couple of films were not irradiated during measurement sessions, but scanned and stored identically to the irradiated films, in order to be used as background validation.

Data analysis of the scanned images was done using MATLAB, in the first instance reading out the intensity values of each images pixels over a region of interest (ROI) in the centre of the films, corresponding to the Roos chamber active area (i.e., a circle of 15.6 mm diameter). The scan images are stored in three channels: red, green and blue. Hence, the pixel intensity values of either or all of these channels may be utilized. The red channel is most sensitive to dose, followed by the green, while the blue channel displays the lowest sensitivity.

The quantity of interest is the optical density OD of the films, subsequently to yield the dose D, given a calibration function $D = D(OD)$. Analogous to the optical density as defined in equation 2.10, the optical density of a film (pixel) is

$$OD = -\log_{10}\left(\frac{I_{i,ch}}{I_0}\right), \tag{3.3}$$

where $I_{i,ch}$ is the ch-channel intensity of pixel index i. The incident (scanner) beam intensity is $I_0 = 65535$, which stems from the colour depth. This is the number of bits available for the brightness gradiation per pixel (per channel), which, in the case of both the scanner and data format used (tagged image file), is 16-bit. 65535 is the highest number that can be represented by an unsigned 16-bit binary number. Thus it becomes apparent that the intensities referred to here may not be associated with a physical unit, but are only of significance in relation.

In this work, three different approaches to obtain the OD from the scans were investigated using calibration films and films at reference conditions, using one, two, or all three channels for readout.

3.4.1 Single channel readout

Both pre- and post-irradiation scan were taken into account, subtracting the resulting optical densities of both scans respectively, to yield the net optical density

$$netOD_{single} = OD_{post} - OD_{pre} = -\log_{10}\left(\frac{I_{post}}{I_{pre}}\right). \tag{3.4}$$

The subscript pre denotes the films prior to irradiation, while $post$ refers to irradiated films. The red channel is the most sensitive, due to the steeper gradient of the optical density OD_{red} over dose, compared to the other channels. Note that, in accordance with equation 3.3, I_0 cancels out.

3.4.2 Dual channel readout

Since the blue channel is less sensitive to dose, including it in the film evaluation together with the red channel should make it possible to decrease effects from thickness variations in the film, due to Beer-Lambert law (equation 2.9). As described by Micke et al. [2011], the optical density was defined using the ratio of these two channels, yielding the net optical density in analogy to the previous case:

$$\begin{aligned} netOD_{dual} &= \frac{OD_{post,red}}{OD_{post,blue}} - \frac{OD_{pre,red}}{OD_{pre,blue}} \\ &= \frac{\log_{10}\left(\frac{I_{post,red}}{I_0}\right)}{\log_{10}\left(\frac{I_{post,blue}}{I_0}\right)} - \frac{\log_{10}\left(\frac{I_{pre,red}}{I_0}\right)}{\log_{10}\left(\frac{I_{pre,blue}}{I_0}\right)}. \end{aligned} \tag{3.5}$$

The division of the logarithm of pixel intensity from both channels was done pixelwise, prior to averaging over the ROI, in order to maintain information on the thickness variations. Though desireable, pixelwise calculations concerning post- and pre-irradiation scans were not maintained, because it was not possible to position the films in the scanner identically.

3.4.3 Triple channel readout

The suggested method by the suppliers ([Micke et al., 2011], further validated by Hayashi et al. [2012]) utilizes all three colour channels, optimising the individual pixel values in order to minimize the differences in the dose results from each channel. In the first instance the optical densities of the calibration films and their corresponding dose values are used to obtain the parameters of a fit function for each channel individually. In contrast to the aforementioned methods, it is in fact just the OD of the post-irradiation scans that is taken into account. Using the fit function, any film scan may be converted into a dose map (i.e. the dose of each pixel is calculated rather than the average over the ROI). The ansatz regarding the following optimization is that the optical density at each point and channel may be split into a dose dependent part D_{ch}^{D} and a dose independent disturbance τ, which contains thickness variations of the active layer and effects from the scan

$$OD_{ch} = OD_{ch}(D)\tau. \tag{3.6}$$

Since the calculated dose should not depend on the choice of channel, the difference between the different channels is minimzed. This is done by minimizing the sum of the squared differences with respect to the disturbance τ, i.e.

$$\frac{d}{d\tau}\sum_{i\neq j}^{3}(D_i - D_j)^2 = 0. \tag{3.7}$$

Thus, dose values are obtained which are optimized with respect to one another.

3.4.4 Choice of calibration function

Concerning the relationship between OD and dose, three different models, introduced in section 2.3.2, were compared using both the single- and the dual-channel readout methods.

For the purposes of this work, the bimolecular model and the gamma-distributed single-hit detector model were adapted slightly. Both equations yield $OD(0) = 0$, which is valid in theory, but does not account for a change in OD between the scans before and after irradiation, which occurs in practice. Films that were not exposed to irradiation, but scanned and stored with all other irradiated films, showed a small decrease in OD. This $OD_{background}$ was accounted for over the entire dose range by adding it to the fit functions as a constant factor, i.e. $OD = OD(D) - OD_{background}$.

OD data for the fit was acquired with EBT3 films measurements of a 179.2 MeV proton beam in water at a depth of 2 cm at seven doses levels between 0 and 3 Gy (calibration film measurements). IC chamber measurements at identical positions

yielded the exact dose. The OD data from calibration films and appropriate dose values obtained from IC measurements were fed to the MATLAB nonlinear least-squares solver (lsqcurvefit), in order to obtain the fit parameters. Concerning the bimolecular and the gamma-distributed single-hit detector model, the maximum OD (OD_{max}) and related variables (namely OD'_{max} and $D_{1/2}$), as seen in equations 2.12 and 2.13, were treated as fit parameters (alongside the other occuring dimensionless parameters).

In order to investigate the quality of different models describing the OD-dose relation, the residuals of the fitted models in relation to the dose values measured with the IC were compared. The bimolecular model marginally showed the best fit for the dose range investigated in this work, as shown in section 4.1.1, and was hence the model of choice concerning further film measurements. It may be noted, however, that the choice of either of the other functions would have negligible effects for the dose range investigated here, due to the near-equivalence of the quality of the functions.

3.4.5 Comparison of readout approaches

The three previously introduced film readout methods, utilizing a single channel, two, or all three channels, were compared in terms of their accuracy. The netOD data used for this comparison was comprised of three individual film measurements per dose. The three readout methods were compared in two seperate ways: Firstly, by treating the dose calculated from the acquired netOD of all three film measurements as a combined dataset, i.e. all pixels (total standard deviation), and secondly by comparing the three individual datasets, i.e., each individual film at given dose (inter film standard deviation).

The total dose uncertainty of the combined dataset was calculated by including the propagated statistical error of each individual film measurement in the statistical error emerging from averaging over all film measurements of same dose, resulting in

$$\sigma^2_{total} = \frac{\sum_{i=1}^{N}(n_i - 1)s_i^2 + n_i(\overline{x}_i - \mu)^2}{\sum_{i=1}^{N} n_i - 1}, \tag{3.8}$$

where i denotes each subset (film), n_i are the number of samples (pixels) per subset (in the calculations made here $n_i \approx 6.5 \times 10^3$), N is the number of subsets, s_i and $\overline{x}_i$ are the standard deviation and mean of each subset, respectively, and finally $\mu = \frac{\sum_{i=1}^{N} \overline{x}_i}{N}$ is the mean of all subsets. For the case here $\overline{x}_i$ corresponds to the mean dose averaged over the ROI, and μ is the average of all three films. Equation 3.8 is known as the unbiased pooled variance, a derivation thereof can be found in

appendix A.

While this result highlights the total uncertainty associated with each dose measurement, information about the spread between individual film measurements of the same dose (subgroups) is washed out. Hence, the variance of the three film measurements at the same dose was calculated neglecting any errors associated with the individual film measurements, i.e.

$$\sigma^2_{inter-film} = \frac{\sum_{i=1}^{N}(\overline{x}_i - \mu)^2}{N-1}. \tag{3.9}$$

For comparison, the same film measurements were used for each readout method. These consisted of the calibration films and films used for measurements of the 148.2 MeV and 252.7 MeV beams at reference conditions (i.e., where no quenching effect is expected). The film dose was calculated from the netOD averaged over the ROI for all three readout methods, using the bimolecular model (eq. 2.12). The deviations from the IC, the total dose uncertainty and the inter-film uncertainty were calculated and used for comparison.

3.4.6 Effects of using 'alien' calibrations

In the general case, a film calibration cannot always be done on the same day as an experiment. The influence of using a calibration obtained at a different point in time, here termed 'alien', was evaluated. Table 3.2 shows the calibrations and validation film measurements performed at different points in time, which were used for the analysis. The validation measurements consist of background films (not irradiated) and measurements at reference conditions.

Table 3.2: Overview over measurement and calibration sessions.

Date	Δt [months]	Measurements	
07/2017	0	calibration t0	/
11/2017	4	/	validation t1
02/2018	7	calibration t2	/
06/2018	12	calibration t3	validation t3

The netOD for the calibrations and the validation measurements were obtained by single channel readout for all three channels. The netOD and dose measured at t0, t2 and t3, were each fitted individually using the bimolecular equation (eq. 2.12). In order to quantify the error made by using an 'alien' calibration, the deviations of the calibrations at t0 and t2, and of the validation measurements, were calculated

with respect to the OD-dose relation from calibration t3. These deviations were calculated for all three channels and compared.

3.5 Characterization of film quenching

3.5.1 Parametrization of relative effectiveness

The under-response of the films is quantified by the relative effectiveness (RE), i.e., the ratio between the dose measured with a film and the applied dose. Throughout this work the RE was calculated as the ratio between the apparent film dose $D_{film}(x)$ and the dose calculated by the MC simulation $D_{MC}(x)$, which was normalized to the Roos chamber, at a depth x

$$RE(x) := \frac{D_{film}(x)}{D_{MC}(x)}. \tag{3.10}$$

For all comparisons between film dose and 'true' dose, including the calculation of RE, the film dose was obtained by reading out the OD of the green channel and calculating the dose via the bimolecular model, in consequence of the findings made in section 4.1.

In order to smooth the RE of the films and acquire more virtual data points, the RE was fitted over depth using the MATLAB internal nonlinear least squares method (lsqcurvefit). This was done for each of the single energy beams and SOBPs individually, taking into account a couple of sigmoidal functions for the fits

$$RE_{logistic}(x) = \frac{a}{1+\exp(b(x-c))} \tag{3.11}$$

$$RE_{algebraic}(x) = \frac{a}{2}\left[1 - \frac{x-c}{\sqrt{b+(x-c)^2}}\right] \tag{3.12}$$

$$RE_{arctan}(x) = \frac{a}{\pi}\left[\frac{\pi}{2} - \arctan(b(x-c))\right] \tag{3.13}$$

$$RE_{tanh}(x) = \frac{a}{2}\left[1 - \tanh(b(x-c))\right]. \tag{3.14}$$

The parameters a, b and c define the maximum value, the steepness of the curve and the x-value at half maximum. The goodness of the fits was evaluated by comparing the χ^2 values.

Using results from the single energy beam measurements, the relationship between RE and residual and relative range was studied, as well as the behaviour of RE over LET_d of protons and of all particles. The different dependencies of RE on LET_d and LET_t were further investigated based on the RE from the SOBP measurements. Fit

function parameters for modeling RE over LET_d were calculated using MATLABs nonlinear least-squares solver. This was done for the data from just single energy beams and SOBPs, respectively, in order to account for and investigate the slight differences between the two datasets. A 3rd order polynomial and a sigmoidal function of the form of equation 3.13 were used as fit functions. A linear relationship, as suggested by Anderson et al. [2019], was also fitted. The uncertainties in the fit parameters were calculated as the square root of the diagonal elements of the variance-covariance matrix

$$\text{Cov} = (J^T J)^{-1} MSE, \tag{3.15}$$

where J is the Jacobian and $MSE = \frac{1}{N_{DOF}} \sum_{i=1}^{n} (RE_i^{meas} - RE_i^{fit})^2$ is the mean squared error, i.e., the sum of the squared errors between all n measured points RE_i^{meas} and the corresponding fit function value RE_i^{fit}, divided by the number of degrees of freedom $N_{DOF} = n - n_p$, where n_p is the number of parameters.

3.5.2 Film quenching corrections

Different film quenching corrections were derived based on LET_d and the LET spectrum. All corrections were calculated using RE obtained from single energy beam measurements, and subsequently validated against the film measurements from the SOBPs. This was also done the other way around, in order to examine the quality of the training data (i.e., single energy beams or SOBPs).

The reader should note that the correction functions explicitly given in this work describe the RE of the films, rather than correcting the film dose in the true sense of the word. In the comparison made in section 4.5, these functions are consequently applied to the nominal (MC) dose, rather than the film dose. The term 'correction' is used nonetheless, since the reciprocals of the functions may be applied to the film dose to obtain the corrected dose.

LET_d correction

The linear fit and arcus tangens fit function, describing the relationship between RE and LET_d, were used to correct the film dose with respect to the LET_d. The parameters used are shown in table 4.4.

In the first instance this correction was simply calculated from the training dataset, and applied to the MC simulations of the validation set. As an alternative approach, in the case of applying the correction to the SOBPs, split SOBP simulations were performed, yielding the depth-dose and LET_d of each individual beam comprising the SOBP. The LET_d correction was then applied to each beam individually, and

the thusly acquired corrected doses added up for each point in depth. This additional approach for the SOBPs is termed split LET_d correction throughout this work.

Spectral LET correction

Instead of modeling the film quenching with average quantities, an ansatz was made involving the entire spectrum of LET-values prevalent in the beam at given depth. Based on the results from the MC simulations introduced in section 3.3.3, yielding the dose over the LET-spectrum for desired depths, weighting factors w_i for each LET-bin i were introduced and applied to the calculation of RE, i.e.,

$$RE_{sim}(w_i) = \frac{\sum_i D_i \, w_i}{\sum_i D_i}. \tag{3.16}$$

The individual w_i were obtained by optimizing the calculated RE_{sim} to the fit of the RE through the measurement points, denoted RE_{meas}, as described in section 3.5.1. Using the smoothed fit function had the advantage of involving simulated spectra at more points in depth than were measured. LET-values up to 100 keV/µm were taken into account, using bin sizes of 0.1 keV/µm. The minimization of

$$\chi^2 = \sum \left((RE_{sim}(w) - RE_{meas})^2 \right) + 10 \sum_i \left((w_i - w_{i+1})^2 \right) \tag{3.17}$$

was performed using MATLABs nonlinear least squares solver, applying a boundary constraint of restricting the w_i to values between 0 and 1.05, and a boundary constraint minimizing the difference between neighbouring w_i and w_{i+1}, i.e. forcing a smooth result over LET. The initial guess values of w were calculated from the nonlinear RE-fit over LET_d, estimating this to be a good starting point.

In addition to this approach obtaining discrete, albeit smoothed weights w_i, an analytic weighting function w_{LET} was sought after, to be applied to an infinitesimal version of equation 3.16,

$$RE_{sim}(w) = \frac{\int D(LET) \; w(LET) \; dLET}{\int D(LET) \; dLET}. \tag{3.18}$$

The analytic dependence of w_{LET} on LET was chosen as

$$\frac{1}{w(LET)} = p_1 + p_2 \left(1 - exp(-(2p_3)^{-2} LET^2) \right), \tag{3.19}$$

since it showed similar behaviour to the weighting factors w_i over LET. The parameters p_1, p_2, p_3 were obtained using MATLABs nonlinear least squares curve-fit function, minimizing

$$\chi^2 = \sum \left((RE_{sim}(w) - RE_{meas})^2 \right). \tag{3.20}$$

Due to faster calculation time the bin size of the LET-spectra was chosen at 0.01 keV/µm. Spectra of depths at which the deviation between IC measurements and MC simulation exceeded 5% were neglected for this approach. This threshold corresponds to a depth of 34.6 mm for the SOBPs, and roughly 30, 150 and 380 mm for the 62.4, 148.2 and 252.7 MeV beam, respectively.

Chapter 4

Results

4.1 Comparison of film analysis

4.1.1 Calibration functions

In order to investigate different models describing the OD-dose relation, the residuals of the fitted models were compared in relation to the dose values measured with the IC. These relative residuals are shown in figure 4.1 for both the single and the dual readout method. The values presented here stem from calibration functions calculated using the red channel, and red and blue channels for the single and dual channel method, respectively.

All three models are similar between 1 and 3 Gy, yielding residuals below 1.5% (single channel) and 2% (dual channel). Only for the lower dose measurements of 0.25 and 0.5 Gy one can observe a difference between the models, with the bimolecular model representing the data marginally better. This statement holds for both the single as for the dual channel readout method. For both methods the residuals of all three models remains smaller than 3.5% at these low doses.

It is worth mentioning that the standard deviation of the measured dose (not shown in the graphs) is larger than the fit residuals, ranging from about 2.5% at 2.5 Gy to over 10% for 0.25 Gy for all three different calibration functions. Since the residuals are smaller than the dose uncertainty over the entire dose range of interest, it follows that all functions are equally good with respect to the measurement accuracy. To maintain readability of the plots in figure 4.1, the dose uncertainties are not shown.

4.1.2 Readout methods

In order to compare the accuracy of the three different readout methods, they were investigated in regard to the resulting deviation from the IC measurements, the film

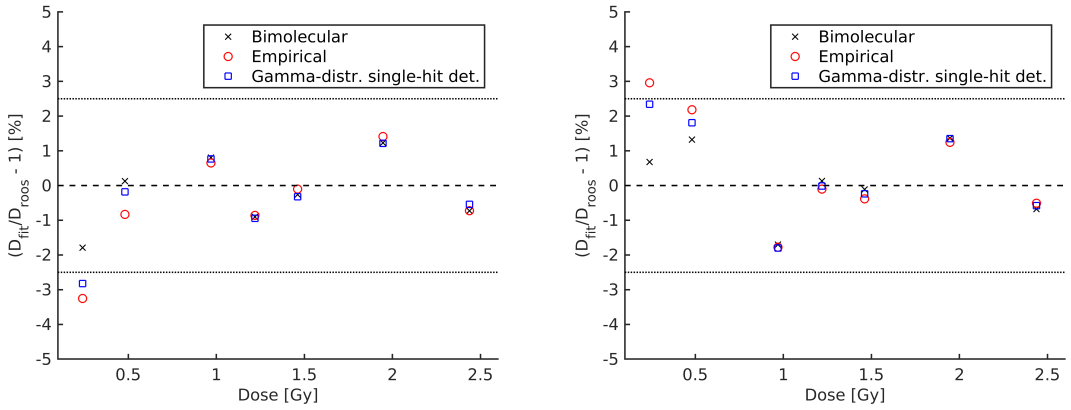

Figure 4.1: Relative dose deviations between calibration function and IC measurements, using different models for the single channel approach (a) and the dual channel readout method (b), respectively.

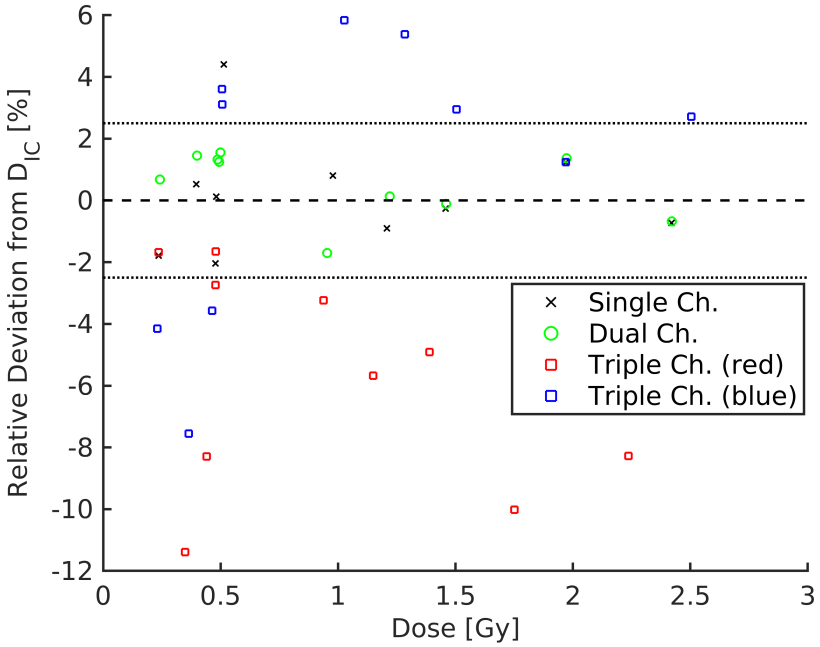

Figure 4.2: Relative deviation from the IC dose measurements for single, dual and triple channel readout methods.

to film dose variance (inter-film variance) and the total dose variance averaged over three individual film measurements, as introduced in section 3.4.5. For the sake of brevity, data from just the red channel (for the single channel readout) and red divided by blue (in the case of the dual channel readout) are plotted in figures 4.2 and 4.3 (though in figure 4.3 the green channel is added too). The same calculations were also done for the other channels and combinations thereof, however, any other choice of channel(s) lead to higher standard deviations for the results of both readout methods, respectively.

Figure 4.2 shows the relative deviation between the dose measured with the IC and the film dose obtained using the single, dual and triple channel method, respectively, calculated using the bimolecuar model in light of the previous section's results. For the single and the dual channel readout the deviations from the dose measured with the IC are below 2.5% over the entire dose-range of interest. However, no clear benefit between the two appears concerning the mean dose. The triple channel readout method was not stable, yielding deviations between 2.5% and 10% for most of the measurement points. It is therefore neglected in the further comparisons. Additionally, the dose variance for the triple channel readout were up to an order of magnitude higher than the other readout methods, which would further diminish the readability if added to the figures.

The inter film standard deviation, describing the film to film variation, is shown in figure 4.3a for the red and green channel obtained by single channel readout, and the dual channel readout (using the red and blue channels). No clear improvement is found when using one of the methods compared to the other, neither is a trend found between them. Independent of the chosen method, the largest inter-film deviations are found below 0.5 Gy, reaching 3-5%.

The total standard deviation from averaging over three dose measurements, calculated taking into account the uncertainty associated with each individual film measurement (equation 3.8), is shown in figure 4.3b for the same readout methods as above. The single red channel yields lower standard deviation for every dose measured, ranging from almost 13% at 0.25 Gy to 2.6% at 2.5 Gy. For the same dose levels the green channel yields 23% and 3.9%. Up to a dose of 1 Gy the uncertainties of dual channel method lie between those of the two single channels, at higher doses dual channel and green channel show similar standard deviations.

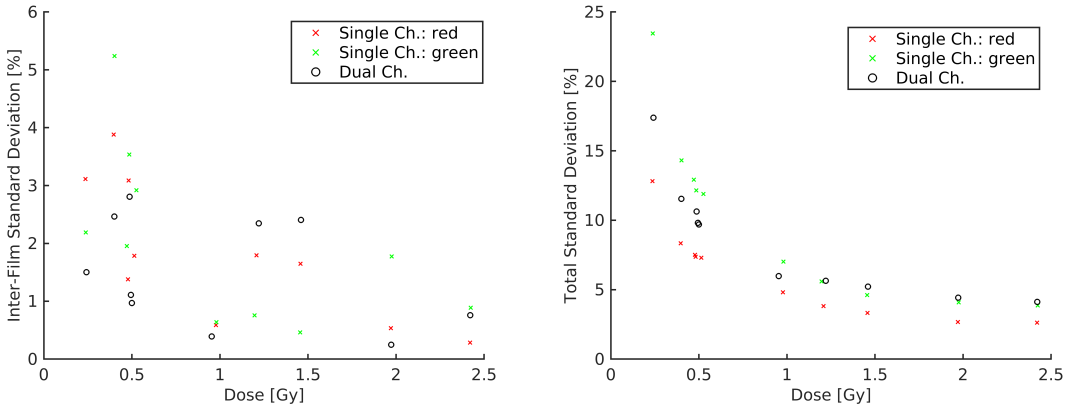

(a) Inter film standard deviation (b) Total standard deviation

Figure 4.3: (a) Comparison of the standard deviation between films from same dose points for single and dual channel readout procedures. (b) Comparison of the total standard deviation for single and dual channel readout procedures, which is equal to the standard deviation of all cummulative pixels from multiple films.

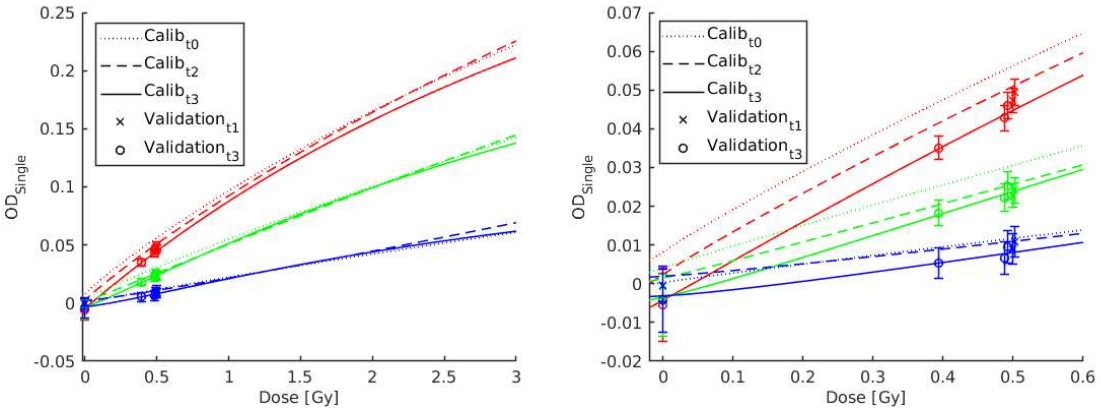

(a) (b)

Figure 4.4: OD-dose relation for all three channels (in their respective colours) for three different calibrations t1, t2 and t3, performed at different times over the space of a year. The film data from validation measurement points (i.e. at reference conditions and non-irradiated films) from both measurement sessions is added to the plots. (b) shows a magnification of (a)

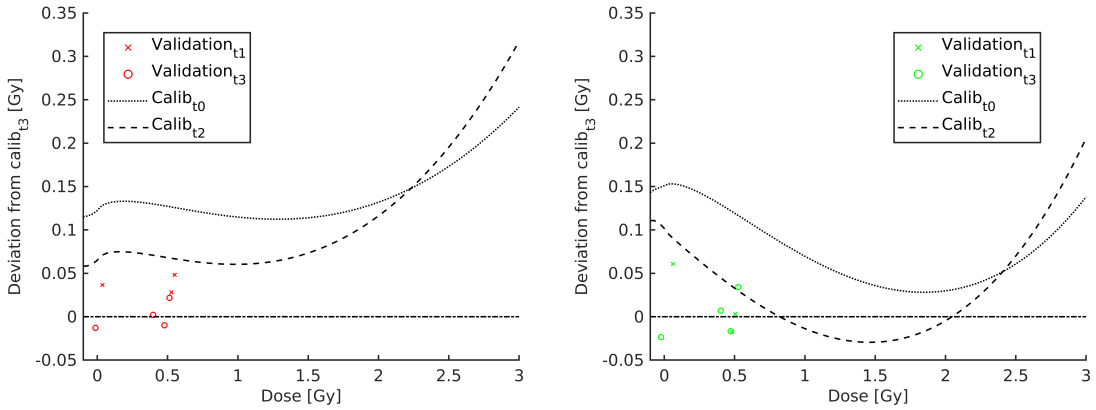

(a) Absolute deviation: red channel

(b) Absolute deviation: green channel

Figure 4.5: Absolute error in Gy, which arises when using an 'alien' calibration, compared to applying the calibration to data measured during the same measurement session, for the red channel (a) and for the green channel (b).

4.1.3 Effects of using 'alien' calibrations

In order to investigate the change of the OD-dose relation over time and the validity of using a calibration obtained at a time $t - \Delta t$ for a measurement session at time t, OD-dose relations obtained at different times were compared. An overview of the measurements used for that purpose is given in table 3.2.

The OD-dose relations obtained from the calibration measurements performed at t0, t2 and t3 using the bimolecular equation, are plotted in figure 4.4, for all three channels. The validation film measurements obtained at t1 and t3 are also shown. The calibration curves show a systematic shift to lower values of OD over time. However, the validation measurements at t1 are not in perfect agreement with this, exhibiting OD-values between those of calibrations t3 and t2 (rather than t0 and t2). Though it should be noted that the uncertainty of the film measurments is of similar magnitude as the differences between the calibration curves.

Figure 4.5 shows the absolute deviations of the OD-dose relation from calibrations t0 and t2, with respect to the OD-dose relation from calibration t3, for the red and the green channel. The deviations between the calibrations, seperated by 5 to 7 months, are in the order of roughly 10% around 0.5 Gy for both channels. Between 0.5 Gy and 3 Gy these differences are smaller for the green channel, compared to the red one. Thus, the choice of calibration in this range will have less of an influence on the results when using the green channel.

The absolute deviations of the validation measurements points at t1 and t3 from the OD-dose relation from calibration t3 are also shown in figure 4.5. For the red channel, the OD values from validation t1 are systematically shifted higher when

using calibration t3, resulting in a higher absolute dose deviation between 0.025 Gy and 0.05 Gy. For the green channel, the validation data from t1 shows likewise large deviation at 0 Gy, however, around 0.5 Gy the data is more centered around 0 Gy deviation.

The parameters of the calibration function

$$D(OD) = D_{1/2} \left(\frac{(OD - OD_{bg})}{OD'_{max} - (OD - OD_{bg})} \right)^{\frac{1}{p}} \tag{4.1}$$

calculated from the measurements performed in the course of calibration t3, are given in table 4.1.

Table 4.1: Fit function parameters used in equation 4.1 for the red and green channel, respectively.

	OD'_{max}	$D_{1/2}$	p	OD_{bg}
Red channel	0.6151	5.5046	1.0203	-0.0042
Green channel	0.4069	5.2865	1.1161	-0.0035

4.2 Characterization of beam quality

4.2.1 Depth-dose and LET

The simulated dose and LET_d of different contributors within the proton beam are compared over the residual range, in this case the distance from R50 in mm, in figures 4.6 - 4.9, for the 62.4 MeV, 148.2 MeV and 252.7 MeV beam. The different particles compared are the primaries, secondary protons, all simulated particles and all particles excluding protons. The latter will further be referred to as heavy particles, since the main dose contribution aside from the protons stems from alpha particles, deuterons, He3 and tritons. The values for R50 obtained from the simulations can be found in table 4.2). It is pointed out that in figures 4.7b, 4.8b and 4.9b, the total dose normalized to the maximal dose is shown qualitatively to locate the Bragg peaks, but not against the vertical axis.

The dose contributions of primary, secondary and heavy particles are shown in figures 4.6 and 4.7. Primary protons dominate the dose contribution for all investigated energies. After a dose build-up at the entrance, the fraction of dose stemming from the secondary protons is fairly constant over the plateau, diminishing near the Bragg peak and dropping to zero at the end of range. The constant level over

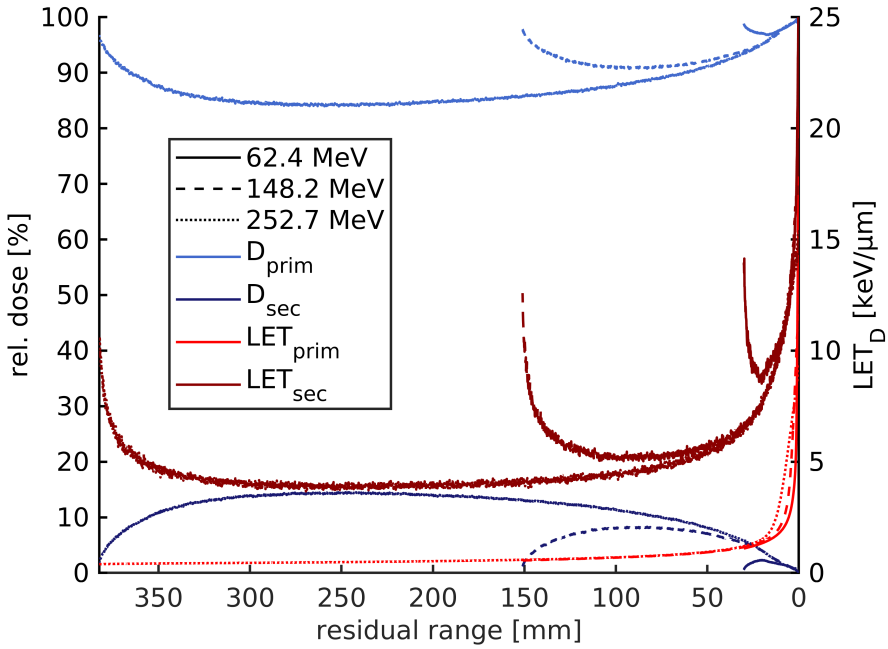

Figure 4.6: Simulated dose and LET_d of a 62.4 MeV, 148.2 MeV and 252.7 MeV beam in water, as a function of residual range. The dose of primary and secondary protons is plotted against the left axis, given in percent of the total dose.

Table 4.2: Simulated ranges (R50 and R80) in water for the 62.4 MeV, 148.2 MeV and 252.7 MeV beam.

Beam energy [MeV]	$R50$ [mm]	$R80$ [mm]
62.4	30.15	29.91
148.2	151.05	150.07
252.7	382.45	380.02

the plateu is reached after a depth of roughly 10-15% of the residual range. The contribution of the secondary protons to the total dose also increases with initial beam energy. For the 252.7 MeV beam the fraction of the total dose deposited by secondary protons reaches a maximum of 14.5%, compared to 8.2% and 2.2% for the 148.2 MeV and 62.4 MeV beam, respectively. In comparison, all other particles (heavy particles) contribute less than 2% of the dose. A dose build-up is not visible for these particles, since they are emitted isotropically (see section 2.1.1). The contribution of these particles over the residual range is similar for all three energies, declining slowly to values of just under 1%, up to residual ranges of 20 to 30 mm. Thus, the dose contribution of these heavy particles is smaller at entrance for lower energies. At a residual range of roughly 15 mm a small peak appears, which is sharper for lower energies, due to the difference in energy spread, followed by a steep dose fall-off. This peak is most likely linked to the nuclear reaction cross-section increasing with lower particle energy down to about 20 MeV (as shown in section 2.1.1), though a detailed investigation is outside of the scope of this work. At the Bragg peak the heavy particle dose contribution is roughly 0.2% for the 252.7 MeV beam, and smaller with lower beam energy.

At small residual ranges the dose contributions of the primary protons become equal within 0.5% for different initial beam energies. For the two higher energy beams this occurs below roughly 25 mm residual range. Below 10 mm all three beams exhibit similar dose contributions from the primaries. The same is also valid for the secondary protons and heavy particles.

Figures 4.8a and 4.8b shows the dose averaged LET of primaries (LET_d^{prim}), secondaries (LET_d^{sec}) and all protons (LET_d^{prot}). The LET_d^{prim} displays a slow increase over most of the range, but rises more dramatically at the Bragg peak and after. For the 62.4 MeV beam it starts at about 1 keV/µm, rising up to 19 keV/µm at R50. For the 148.2 MeV, and 252.7 MeV beams the LET_d^{prim} is in the range of 0.5 to 12 keV/µm and 0.4 to 9 keV/µm, respectively. The LET_d^{sec} is higher, ranging from approximately 9 to 25 keV/µm for the 62.4 MeV beam, 5 to 20 keV/µm for the 148.2 MeV beam, and 4 to 15 keV/µm for the 252.7 MeV beam, due to the lower energy of the secondary protons. However, it is worth keeping in mind the dose contributions of primary and secondary protons when considering the LET_d. When looking at the LET_d^{prot} of all protons, the contribution of the secondary particles manifests itself in the plateau, where the LET_d^{prot} becomes maximally 0.5 keV/µm (252.7 MeV), 0.35 keV/µm (148.2 MeV) and 0.2 keV/µm (62.4 MeV) higher than that of the primaries. In percent the LET_d^{prot} along the plateau is around 100-115% (252.7 MeV), 50-60% (148.2 MeV) and 10-15% (62.4 MeV) higher than the LET_d^{prim}. In absolute terms, the LET_d^{prot} is roughly 1 keV/µm in the plateau for all examined energies. Around the Bragg peak the LET_d^{prot} of protons becomes identical to that of the primary particles, thus exhibiting the same differences between

the different beam energies as is the case for the primaries.

The LET_d of all particles (LET_d^{all}), all protons and heavy particles (LET_d^{heavy}) are shown in figures 4.9a and 4.9b. LET_d^{all} and LET_d^{heavy} differ from the LET_d^{prot} by one and two orders of magnitude, yielding values of magnitudes around 10 keV/µm and 500 keV/µm, respectively. The LET_d^{all} slowly decreases as a direct result of the decrease in dose contribution of the heavier particles, converging with the LET_d^{prot} near the Bragg peak when the dose contribution of the heavy particles drops to (almost) zero.

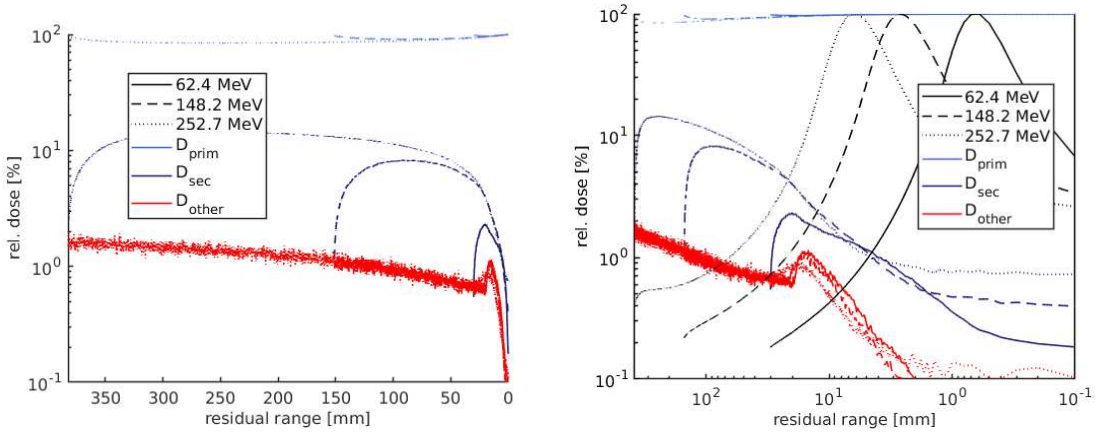

(a) (b)

Figure 4.7: Simulated dose of primary protons, secondary protons and all other particles, for a 62.4 MeV, 148.2 MeV and 252.7 MeV beam, respectively, in percent of the total dose (logarithmic scale). The depth is shown in terms of the residual range. Figure (b) shows the data over the residual range on a logarithmic scale, with the total dose additionally plotted merely qualitatively to locate the Bragg peak (i.e., not against the given vertical axis).

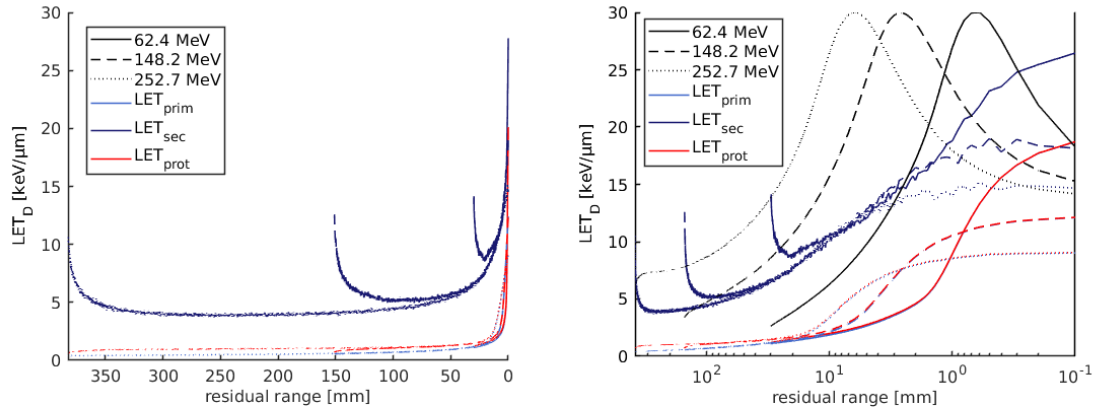

(a) (b)

Figure 4.8: Simulated LET_d of primary, secondary, and all protons, for the three different beam energies as a function of residual range. Figure (b) shows the data over the residual range on a logarithmic scale, with the total dose added to locate the bragg peak.

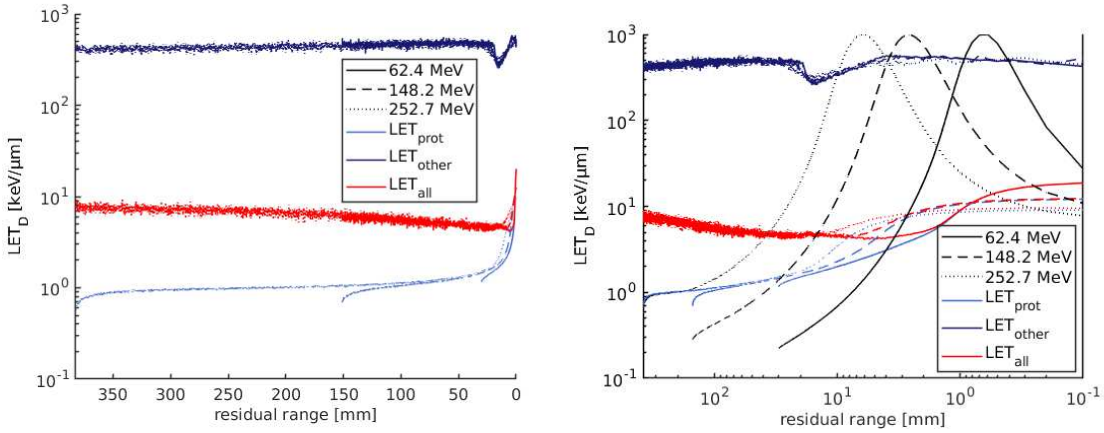

(a) (b)

Figure 4.9: Simulated LET_d for protons, all other particles, and all particles (including protons) for the individual beam energies over the residual range. Figure (b) shows the data analogously to the previous two figures.

Figure 4.10 shows the differences between LET_d^{prot} and LET_t^{prot} for the SOBPs over depth, for all three simulated beams. Since $b1$ is made up of beams of similar (lower) energies (for SOBP composition, see section 3.1.3), the fluence and contributions to dose are made up of particles of similar energy. $b2$ and $b3$ have a contribution from a higher energy 252.7 MeV beam. Thus, for the LET_t^{prot}, the low energy/high LET protons (depositing more energy) are drowned out by the high energy/low LET protons of the high energy beam. As a result, the LET_t^{prot} is dramatically lower, reaching merely 12% ($b2$) and 6% ($b3$) of the LET_d^{prot} at the distal fall-off where

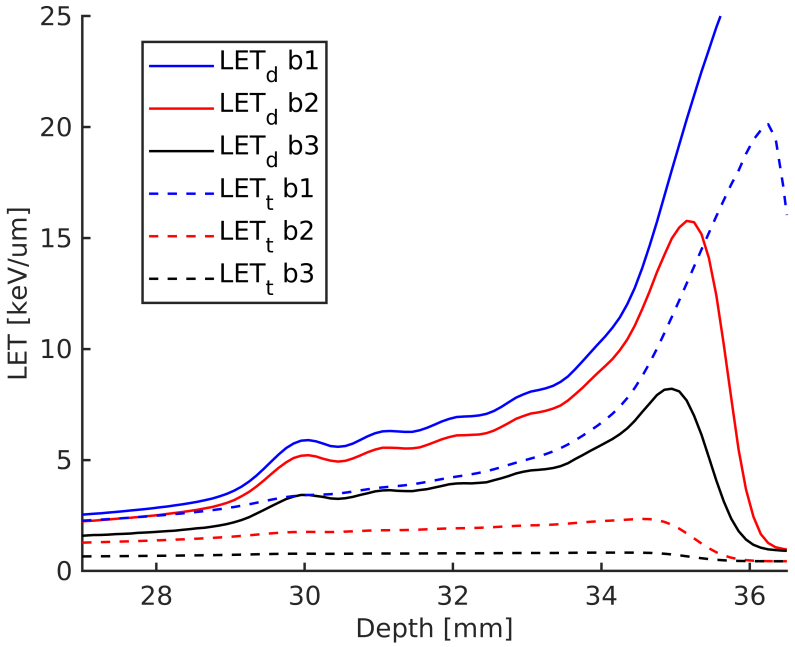

Figure 4.10: Comparison of LET_d^{prot} and LET_t^{prot} over depth for the three different SOBPs.

LET_d^{prot} is maximal.

4.2.2 Spectral analysis

Figure 4.11 shows multiple simulated LET-spectra of the 62.4 MeV beam for different depths in water. It illustrates the choice of positions at which the spectra were calculated, with a higher resolution at larger depths where the LET_d increases. The increasing spread of LET due to the energy spread is also evident.

Figures 4.12a and 4.12b show LET-spectra at an LET_d of (6.6 ± 0.2) keV/µm, for the monoenergetic beams and SOBPs, respectively. The single energy beam spectra exhibit maximal dose contribution at increasing LET of 2.4, 3.0 and 4.7 keV/µm with decreasing beam energy, followed by larger dose contributions from particles of higher LET with increasing beam energy. The SOBP $b1$ has a single peak at 2.9 keV/µm (unimodal distribution), while the other two SOBPs, with local peaks at 3.4 keV/µm ($b2$) and 9 keV/µm ($b3$), have an additional sharp global peak at 0.4 keV/µm due to the contribution of the high energy beam (multimodal distributions). In contrast to the similar shape of the monoenergetic beam spectra, the SOBPs exhibit different LET spectra yielding the same LET_d.

The reader is reminded that the simulations of single energy beams and SOBPs

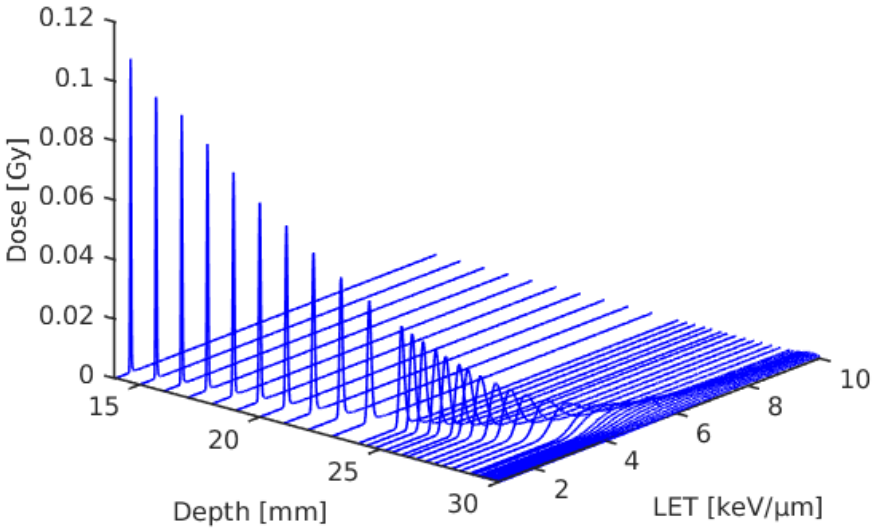

Figure 4.11: LET spectra of a 62.4 MeV beam over depth.

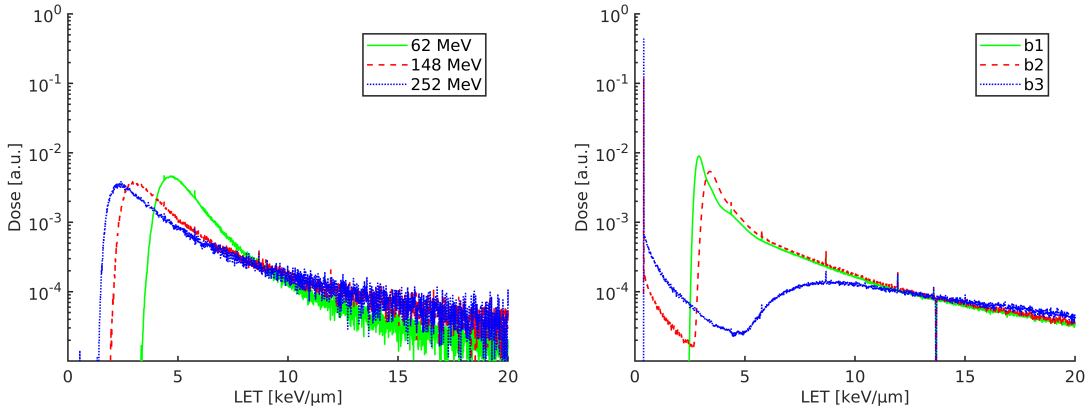

(a) (b)

Figure 4.12: LET-spectra of single energy beams (a) and SOBPs (b) at constant $LET_d = 6.6\,\mathrm{keV/\mu m}$, normalized to the total dose.

differ slightly, as explained in section 3.3.2. This is the reason the single energy beam spectra display a higher variance, as seen in figure 4.12.

4.3 Experimental vs simulation results

4.3.1 Single energy beams

Figure 4.13 shows the measurements from EBT3 films, Roos IC and the simulated dose as a function of depth for the three investigated single energies. The under-response of the films near the Bragg peak is clearly visible, reaching roughly 10% (252.7 MeV), 15% (148.2 MeV), and 30-40% (62.4 MeV) at the Bragg peak. At R50 these values increase to approximately 15% (252.7 MeV), 30% (148.2 MeV), and 70% (62.4 MeV). The dose uncertainty of the film measurements was calculated by propagating the statistical error of the intensity emerging from averaging over the pixels in the ROI.

The deviation between IC measurement and MC simulation is displayed in figure 4.14. The uncertainties applied to the IC measurements stem from the position uncertainty due to the measurement setup, which was estimated to be approximately 0.1 mm. The good accordance between IC and MC is lost only for a few measurement points near the end of range, i.e. in the presence of a steep gradient. The 62.4 MeV beam deviated less than 5% up to a depth of 30 mm, reaching about 18% at greater depths. Similarly the uncertainty of these deviations remains below 5% up to 29.7 mm depth. For the 148.2 MeV beam the deviations are within 6% over the entire depth, along with the measurement uncertainty. In the case of the 252.7 MeV beam the deviations and associated uncertainties are below 2% up to 380 mm in depth.

Figure 4.13 shows the measurements from EBT3 films, Roos IC and the simulated dose as a function of depth for the three investigated single energies. The under-response of the films near the Bragg peak is clearly visible, reaching roughly 10% (252.7 MeV), 15% (148.2 MeV), and 30-40% (62.4 MeV) at the Bragg peak. At R50 these values increase to approximately 15% (252.7 MeV), 30% (148.2 MeV), and 70% (62.4 MeV). The dose uncertainty of the film measurements was calculated by propagating the statistical error of the intensity emerging from averaging over the pixels in the ROI.

The deviation between IC measurement and MC simulation is displayed in figure 4.14. The uncertainties applied to the IC measurements stem from the position uncertainty due to the measurement setup, which was estimated to be approximately

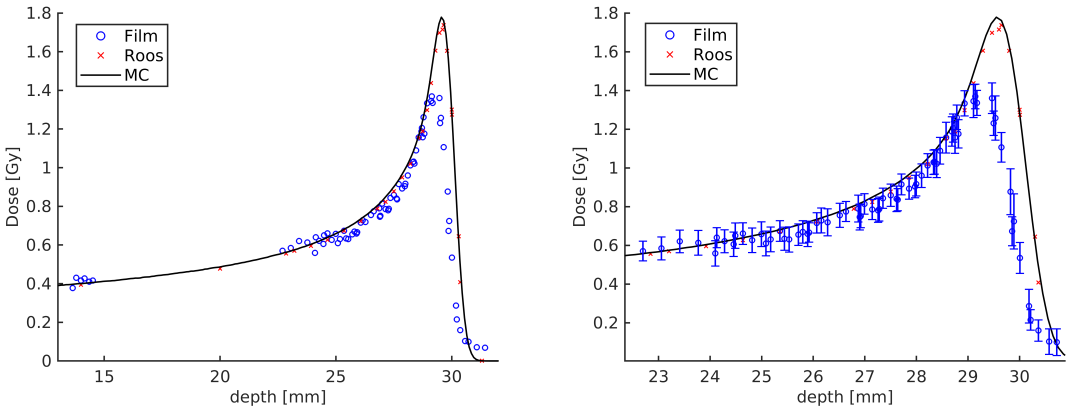

(a) 62.4 MeV beam

(b) 62.4 MeV Bragg peak detail

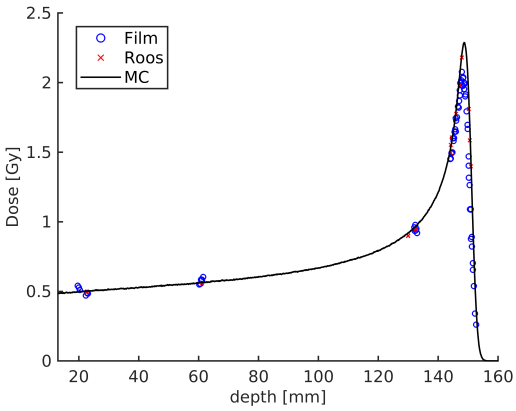

(c) 148.2 MeV beam

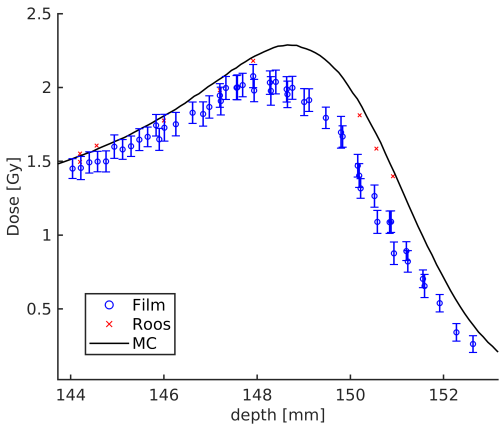

(d) 148.2 MeV Bragg peak detail

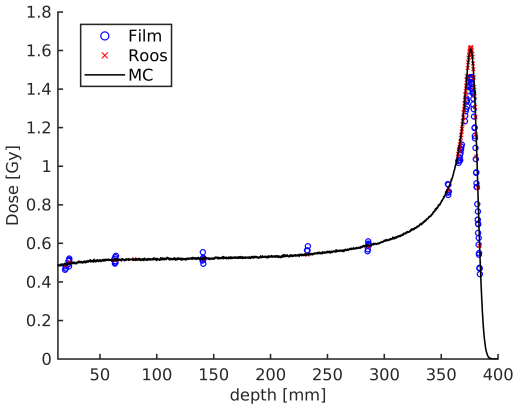

(e) 252.7 MeV beam

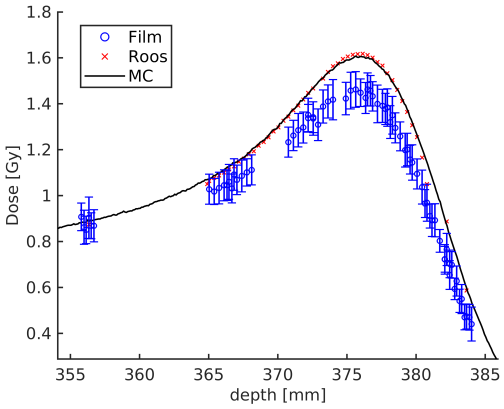

(f) 252.7 MeV Bragg peak detail

Figure 4.13: The plots (a), (c) and (e) show the full simulated depth dose curves (Bragg curves) of a 62.4 MeV, 148.2 MeV and 252.7 MeV beam, including the measurements performed with the Roos chamber and the films. A magnification of the Bragg peak region is plotted in the right column, including the uncertainties of the film measurements (1 sigma confidence interval).

0.1 mm. The good accordance between IC and MC is lost only for a few measurement points near the end of range, i.e. in the presence of a steep gradient. The 62.4 MeV beam deviated less than 5% up to a depth of 30 mm, reaching about 18% at greater depths. Similarly the uncertainty of these deviations remains below 5% up to 29.7 mm depth. For the 148.2 MeV beam the deviations are within 6% over the entire depth, along with the measurement uncertainty. In the case of the 252.7 MeV beam the deviations and associated uncertainties are below 2% up to 380 mm in depth.

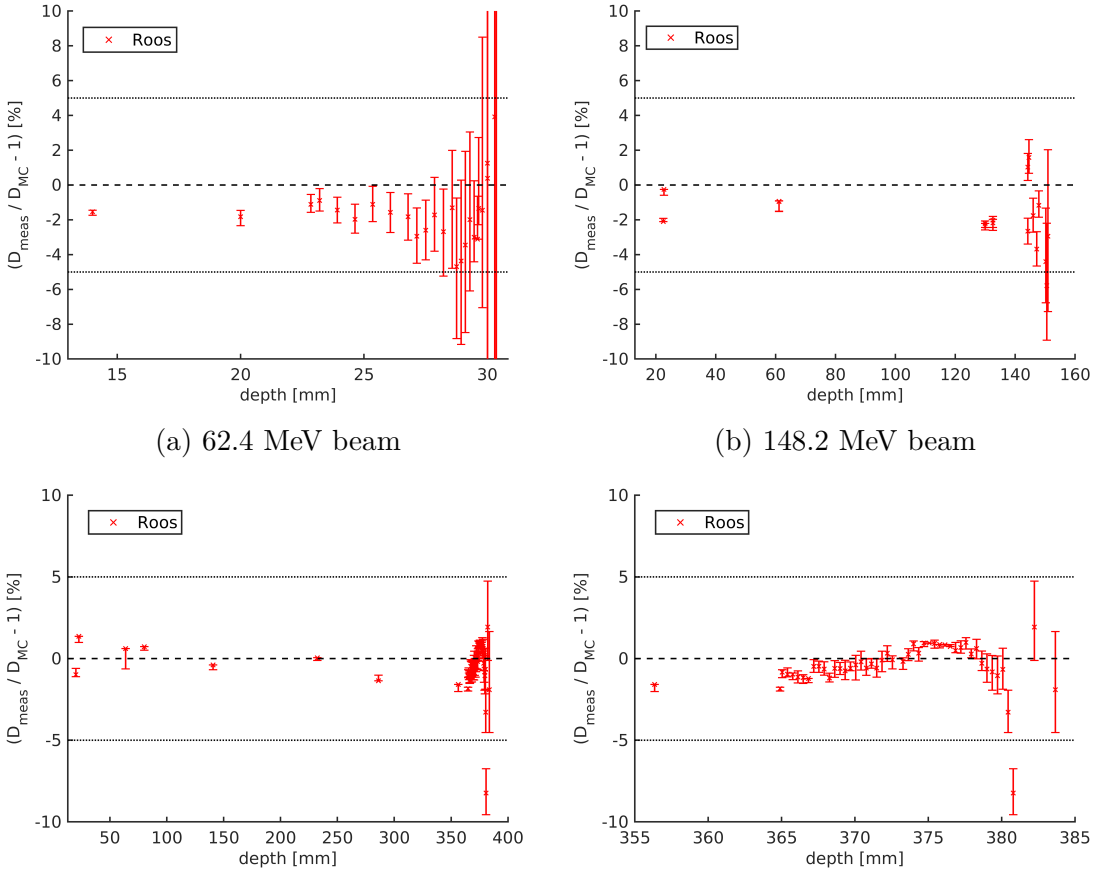

(a) 62.4 MeV beam

(b) 148.2 MeV beam

(c) 252.7 MeV beam

(d) 252.7 MeV Bragg peak detail

Figure 4.14: Residuals of the MC simulated dose with respect to the Roos chamber measurements, for the three investigated beam energies. The included uncertainty intervals stem from the assumed position uncertainty of 0.1 mm.

4.3.2 SOBPs

Figure 4.15 shows the simulated and measured depth dose distribution of the three SOBPs (introduced in section 3.1.3). Film measurements of $b1$ and $b2$ exhibit a similar under-response over the modulated peak region, increasing from 10% to 30%,

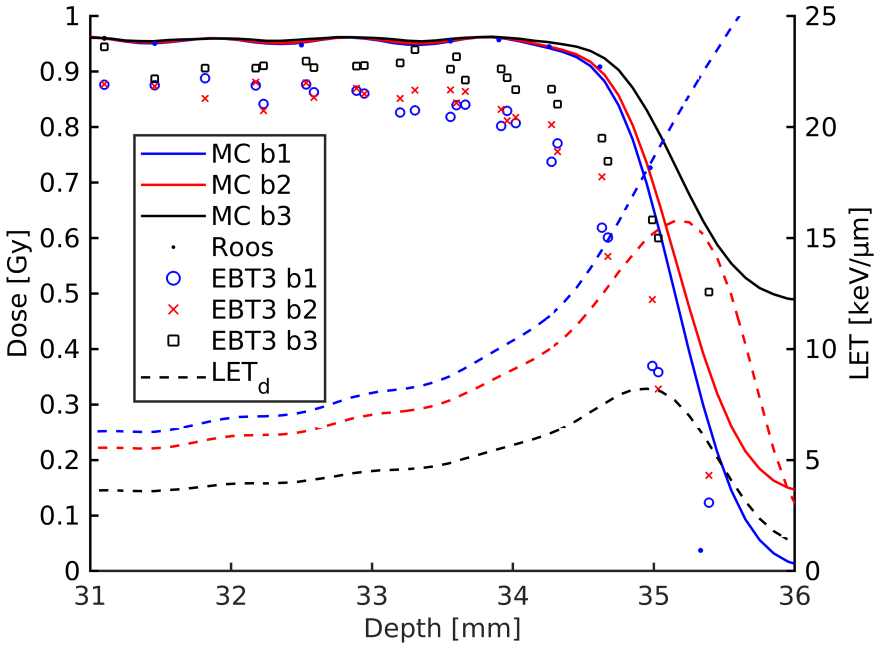

Figure 4.15: MC simulated dose and LET_d^{prot} over depth for three SOBP beams, including roos chamber and EBT3 film measurements.

whereas the under-response of the $b3$ measurements is systematically lower, ranging from roughly 5% to around 15-20% over the modulated peak. The uncertainties are not added to the plot for readability. Over the modulated peak they are roughly 5% for all three beams, increasing at the fall-off to 10-40% ($b1$), 10-20% ($b2$) and 7% ($b3$), depending on the dose gradient.

The deviations between IC and MC simulation for $b1$ are shown in figure 4.16, remaining below 2% up to a depth of 34.6 mm, i.e., over the entire modulated peak. Along the distal fall-off the deviations become larger, ranging from 8% at 35 mm to almost 90% at 35.3 mm. The positioning-induced uncertainty remains below 1% over the peak region, but increases due to the steep gradient at the fall-off to roughly 20% (35 mm).

4.4 Relative effectiveness

4.4.1 Parametrization over depth

The fit functions of the RE over depth, together with the film measurement points, are shown in figures 4.17 and 4.18. The uncertainties in RE are larger than the differences between the sigmoidal functions, deeming any of them sufficient to describe the RE over depth. Nevertheless, for the 62.4 MeV beam and all three SOBPs

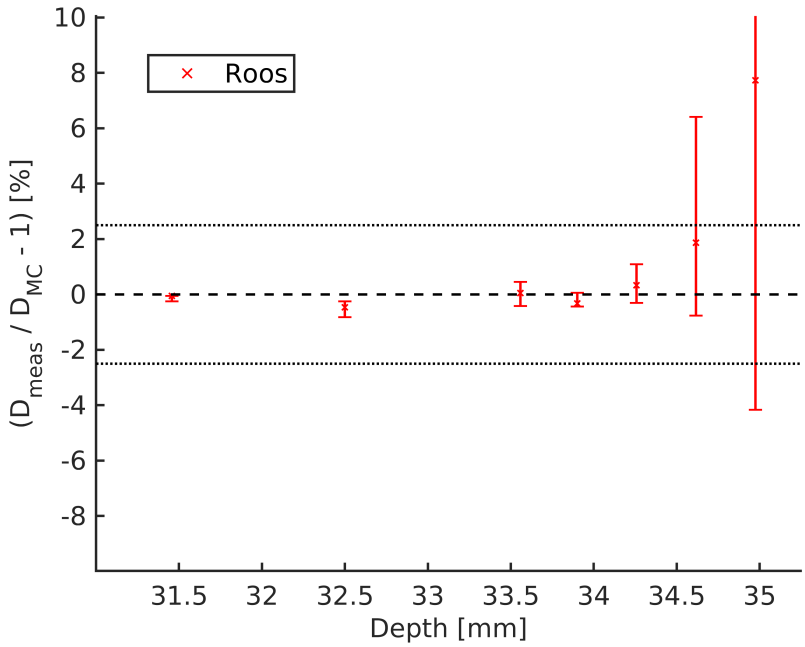

Figure 4.16: Deviation between MC simulated dose and Roos chamber measurements for the SOBP *b*1, including the positioning-induced dose uncertainty.

the logistic function 3.11 ($RE_{logistic}$) resulted in the lowest χ^2 value, while for the 148.2 MeV and 252.7 MeV beams the function 3.12 ($RE_{algebraic}$) was the best to describe the RE over depth. The parameters obtained for the best fits of the individual beams can be found in table 4.3.

Table 4.3: Fit function parameters used in equations 3.11 and 3.12, for the different beams and functions.

$RE_{logistic}$	a	b	c
62.4 MeV	0.971	3.007	29.886
SOBP b1	0.914	1.727	35.348
SOBP b2	0.911	1.966	35.362
SOBP b3	0.971	1.043	36.567

$RE_{algebraic}$	a	b	c
148.2 MeV	1.018	21.942	153.220
252.7 MeV	1.006	234.912	395.314

4.4.2 Residual and relative range

In figure 4.19 the RE is shown over the residual range for the three single energy beams. The steepness with which the RE declines for each of the beams differs between the energies. The lower the initial beam energy, the steeper the decline of RE over the residual range.

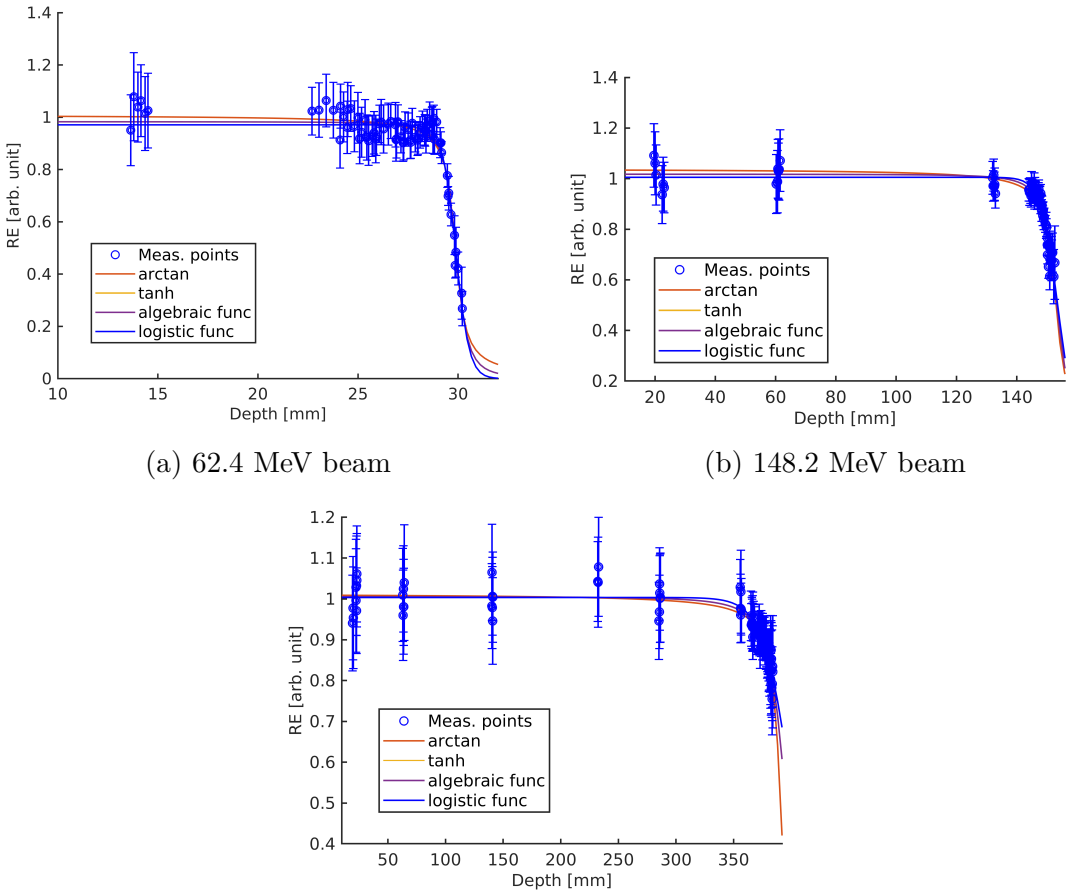

(a) 62.4 MeV beam

(b) 148.2 MeV beam

(c) 252.7 MeV

Figure 4.17: Fit functions for all the single energy beams over depth: 62.4 MeV (a), 148.2 MeV (b) and 252.7 MeV (c).

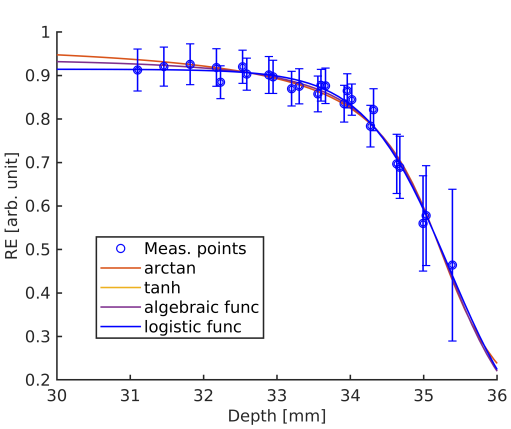

(a) SOBP beam 1

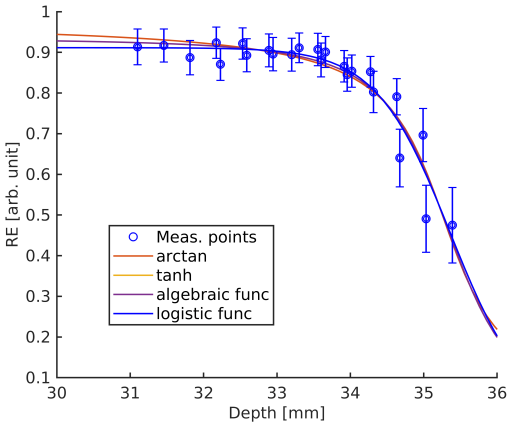

(b) SOBP beam 2

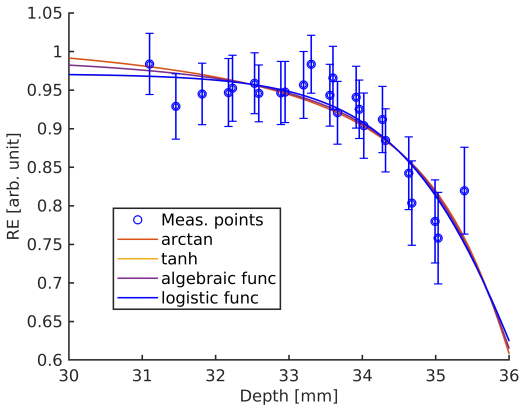

(c) SOBP beam 3

Figure 4.18: Fit functions over depth for all the SOBPs.

Figure 4.20 shows the RE plotted over the relative range, $r_{rel} = \frac{depth}{R50}$. Up to a relative range of approximately 80% the smoothed RE of each beam individually changes by less than 1%. In this region the smoothed RE differs by maximally 5% between the beams, converging between a relative range of 80% to 95%, and diverging thereafter.

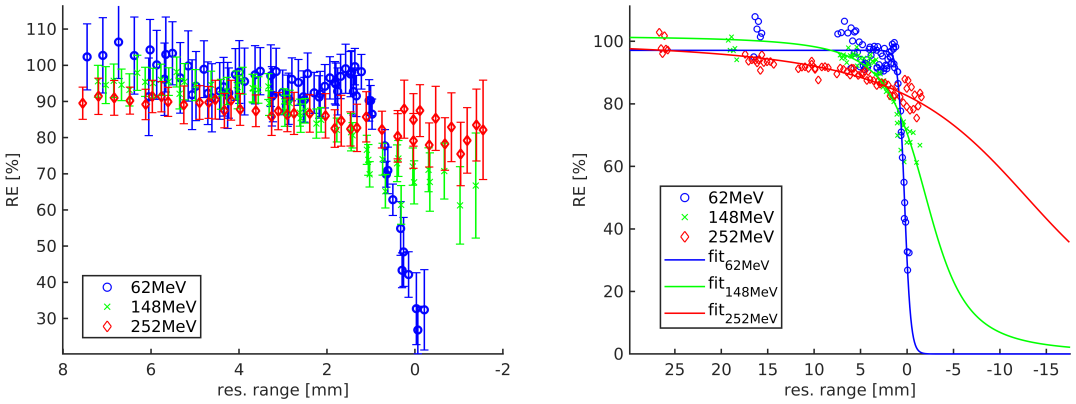

(a) (b)

Figure 4.19: RE over residual range (R50) for the 62.4 MeV, 148.2 MeV and 252.7 MeV beam. (b) includes the fit functions for the three beams.

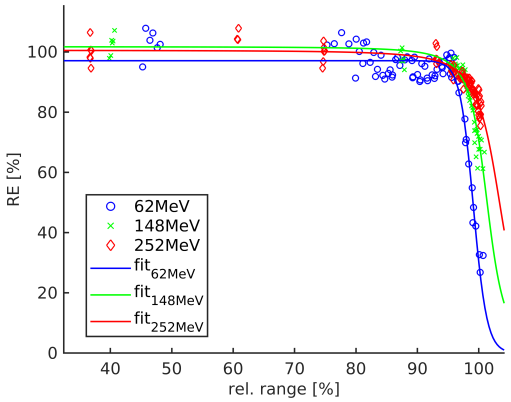

Figure 4.20: RE over relative range (R50) in [%] for the 62.4 MeV, 148.2 MeV and 252.7 MeV beam, including the fit functions for the three beams.

4.4.3 Dependence on LET

The RE over LET_d^{prot} for the single energy beams is shown in figure 4.21. There is a clear trend for the RE over the LET_d^{prot}, dropping from approximately 100% around 1 keV/µm to about 33% for LET_d^{prot}-values of roughly 21 keV/µm. The RE uncertainty was calculated including the propagated error stemming from the averaging

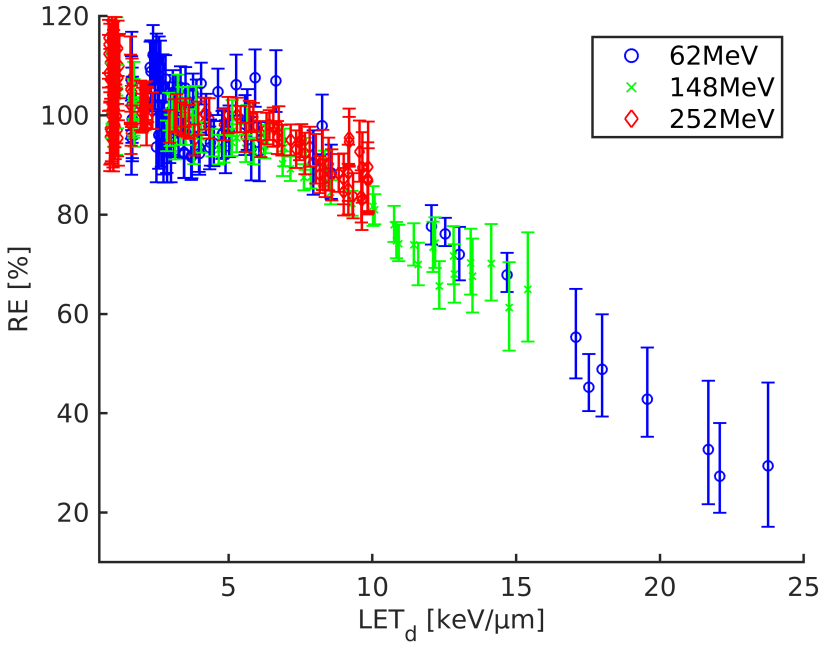

Figure 4.21: Relative effectiveness over LET_d^{prot} for the 62.4, 148.2 and 252.7 MeV beam, using the green channel.

over the ROI of the films σ_{film}, and the dose uncertainty induced by the position uncertainty σ_{pos}, i.e. $\sigma^2 = \sigma_{film}^2 + \sigma_{pos}^2$.

Figure 4.22a shows the RE as a function of LET_d^{prot} for the SOBPs. The three beams are in approximate agreement, i.e., the differences are within the measurement uncertainty, apart from a few measurement points. These outliers don't occur systematically above a specific LET_d^{prot}-value. For both $b2$ and $b3$ they are points near the distal fall-off (with different LET_d^{prot}).

In comparison, plotting the RE over LET_t^{prot} (figure 4.22b) yields very different results for the three beams, respectively. For beams $b2$ and $b3$ the RE is not a function of LET_t^{prot}, which remains approximately constant over all measurement points, while yielding varying RE-values. The uncertainty in LET_t^{prot} is induced by the position uncertainty of the films, while the uncertainty in RE is σ_{film}.

Figure 4.23 shows the RE over the LET_d^{all} averaged over all particles for the three single energy beams, with the fits of RE calculated over depth (see section 4.4.1) added to guide the eye. Between 5 and 10 keV/µm the relationship between RE and LET_d^{all} is not well-defined for the highest energy beam. As shown in section 4.2.1, the LET_d^{all} initially decreases over residual range for the higher energy beams before increasing, resulting in a loss of bijectivity. The case is similar for the lower energy beams, though the LET_d-bandwidth for which the relationship is ill-defined

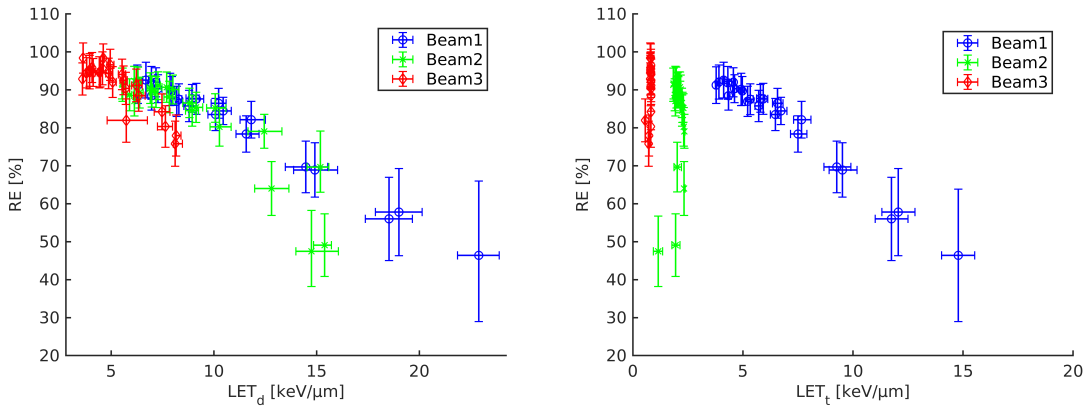

(a) (b)

Figure 4.22: Relative effectiveness over LET_d^{prot} (a) and over LET_t^{prot} (b) for all three SOBPs

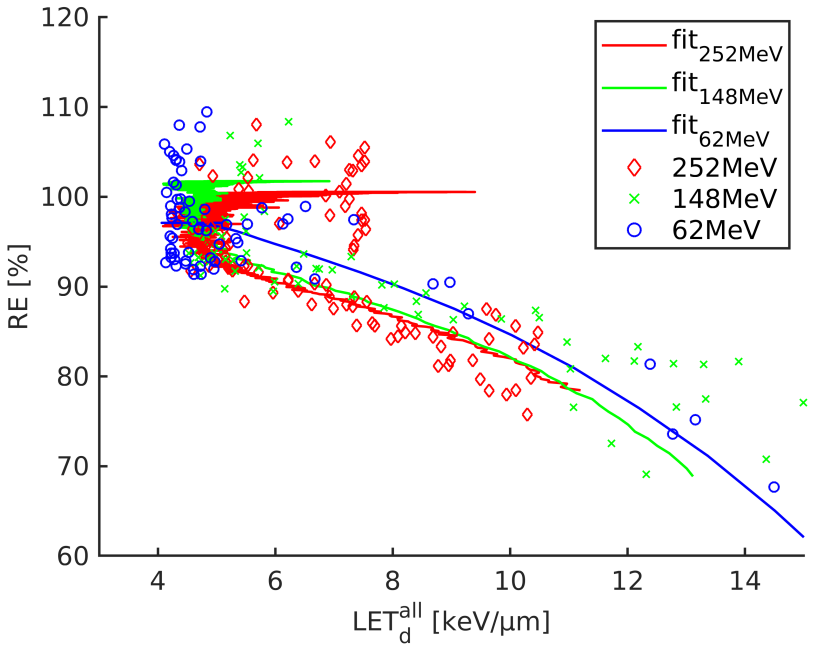

Figure 4.23: Relative effectiveness over LET_d^{all} for the three quasi-monoenergetic beams.

becomes smaller with decreasing beam energy. The measurement uncertainties are not added to the plot for visibility. While the uncertainties of all points between 5 and 10 keV/µm overlap, points are centered around distinctly different RE for the same LET_d^{all}, as is additionally highlighted by the RE-fits.

4.4.4 Parametrization over LET_d

Figures 4.24a and 4.24b show the fit functions for RE over LET_d^{prot}, calculated using the results from only the single energy beams and from only the SOBPs, respectively. All film measurements are included in both plots. The parameters for the functions calculated using the different training data sets are given in tables 4.4 and 4.5. Fitting the data with a 3rd order polynomial,

$$RE_{poly}(LET_d) = p_0 + p_1 LET_d + p_2 LET_d^2 + p_3 LET_d^3, \tag{4.2}$$

leads to the best fit in terms of χ^2, though the shape varies considerably between the two training data sets. The parametrized arcus tangens,

$$RE_{arctan}(LET_d) = \frac{p_0}{\pi}\left[\frac{\pi}{2} - \arctan(p_1(LET_d - p_2))\right], \tag{4.3}$$

leads to fits of very similar quality as the polynomial, while maintaining similar shape for both fit scenarios. The quality of the linear fit,

$$RE_{lin}(LET_d) = p_0 + p_1 LET_d, \tag{4.4}$$

is comparable when fitted to the SOBPs, but diminished when applied to the RE of the single energy beams.

Table 4.4: Fit function parameters as used in figure 4.24a

	p_0	p_1	p_2	p_3
RE_{lin}	1.047 ± 0.045	-0.0272 ± 0.0007		
RE_{atan}	1.214 ± 0.018	0.1127 ± 0.0071	14.84 ± 0.25	
RE_{poly}	1.015 ± 0.008	-0.015 ± 0.004	(-5.2 ± 4.9) 10^{-4}	(-1.5 ± 1.6) 10^{-5}

For the LET_d^{prot}-range up to 25 keV/µm, the absolute difference between the linear fits from the two datasets drops from roughly 3% RE to 2%. The linear fit generated from the single energy beam results is consistently lower by 3% to 5% compared to the linear fit calculated from the SOBP results.

Up to roughly 12 keV/µm the difference between the two arcus tangens fits is smaller than that of the linear fits, becoming larger for higher LET_d^{prot}-values, reaching a difference of 10% in terms of RE at around 20 keV/µm.

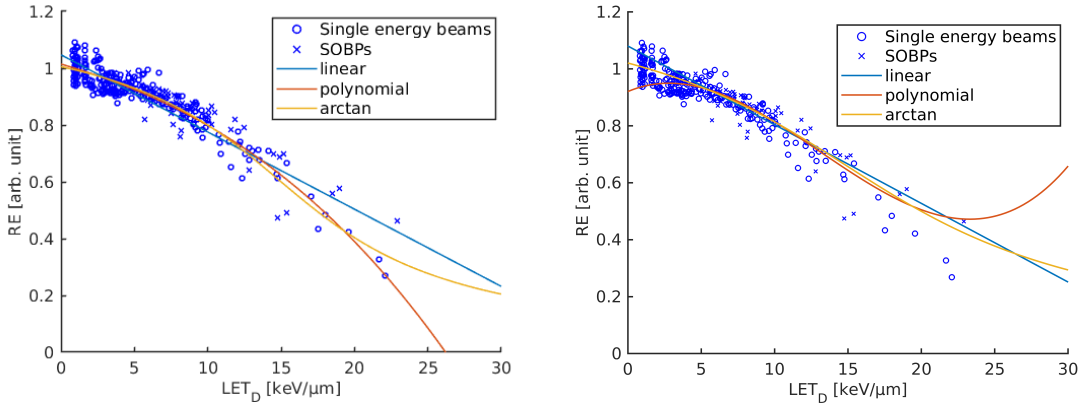

(a) (b)

Figure 4.24: Linear, polynomial and arcus tangens fit functions of RE over LET_d^{prot}, calculated using the results from single energy beams (a) and the SOBPs (b). All measurement points are shown in both plots.

Table 4.5: Fit function parameters as used in figure 4.24b

	p_0	p_1	p_2	p_3
RE_{lin}	1.080 ± 0.013	-0.0276 ± 0.0015		
RE_{atan}	1.315 ± 0.089	0.0788 ± 0.0125	14.973 ± 1.445	
RE_{poly}	0.921 ± 0.058	0.0217 ± 0.0178	-0.0043 ± 0.0016	(1.1 ± 0.4) 10^{-4}

4.5 Comparison of film corrections

4.5.1 Spectral corrections

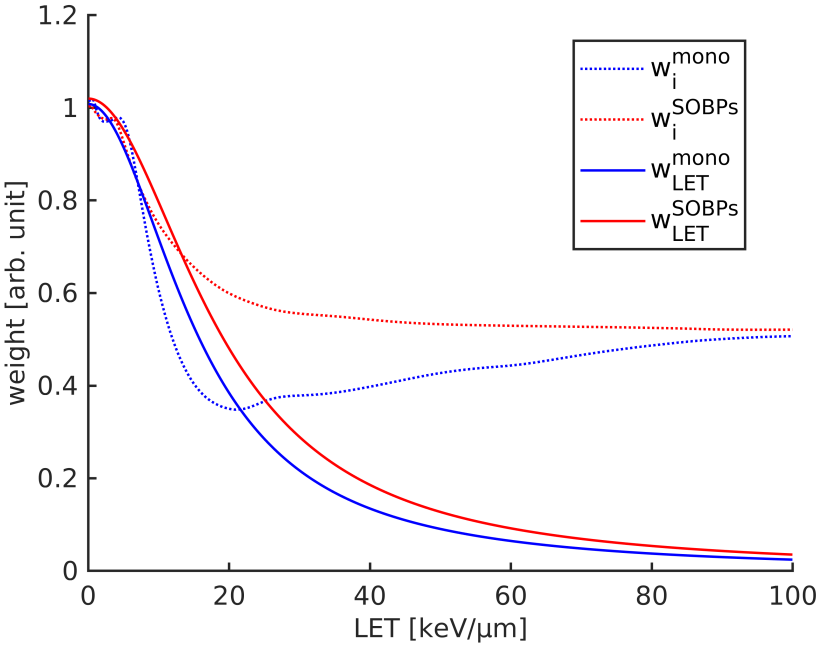

Figure 4.25: Weights over LET calculated by discrete optimization, denoted w_i, and optimization of the parameters of the function $\frac{1}{w(LET)} = p_1 + p_2\,(1 - exp(-(2p_3)^{-2}LET^2))$, denoted w_{LET}, using the monoenergetic beam and SOBP measurements as training data.

Figure 4.25 shows the weights over the LET spectrum from 0 to 100 keV/µm, calculated as described in section 3.5.2. Both the weights w_i from discrete optimization and the optimized function w_{LET} are plotted, each calculated using the RE from the monoenergetic beams and the SOBPs, respectively. The discrete weights remain at higher values between 0.35 and 0.6 from approximately 20 keV/µm onwards, whereas the functions converge toward zero. The weights based on the SOBP measurements show a comparable to larger effectiveness over the entire spectrum, compared to those based on the monoenergetic beams.

The function w_{LET} drops to 0.8 at roughly 8 and 10 keV/µm, and to 0.5 at around 16 and 19 keV/µm, calculated from the different training data sets, respectively. Up to an LET of 4 keV/µm the weights of all four functions display values between 0.95 and 1.02. In this region the discrete weights don't decrease monotonically, but show a small bump around 4 to 5 keV/µm.

For the calculation of the presented w_{LET} functions, only spectra of depths at which the IC measurements and simulations show deviations below than 5% were

used. When additionally taking into account spectra associated with larger measurement uncertainties, the weight function shows resemblance to a heaviside function with the step at 11 to 12.5 keV/µm (depending on the data set used).

The discrete optimization is very dependent on the boundary conditions. Without the smoothing condition, the w_i become very noisy between 20 and 100 keV/µm.

Table 4.6: Weight function parameters as used in figure 4.25

	p_1	p_2	p_3
w_{LET}^{mono}	756.79	9217.33	0.99
w_{LET}^{SOBPs}	540.05	3212.82	0.98

4.5.2 Corrections calculated from single energy beams

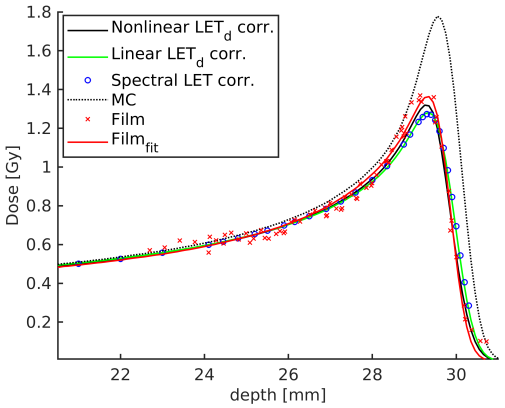

(a) 62.4 MeV: Corrections

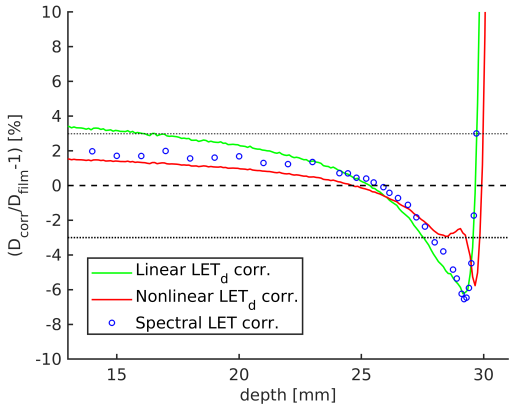

(b) 62.4 MeV: Residuals

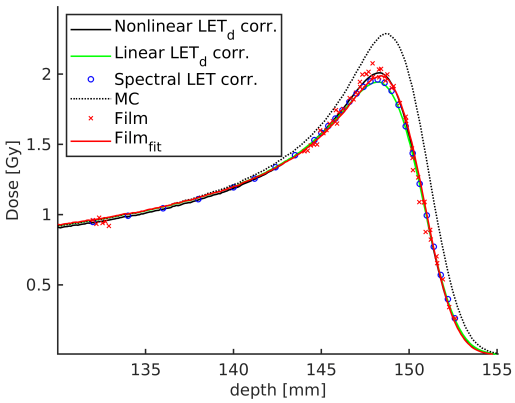

(c) 148.2 MeV: Corrections

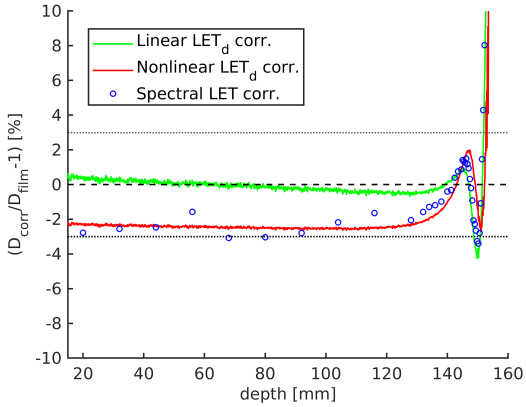

(d) 148.2 MeV: Residuals

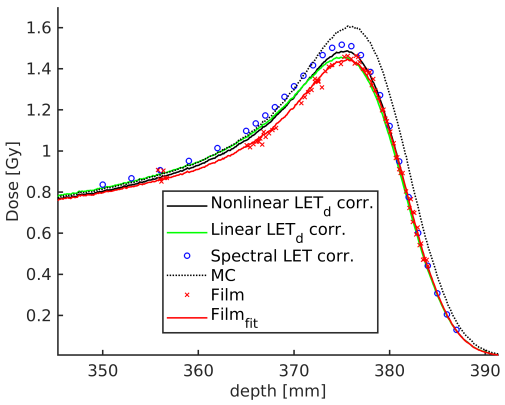

(e) 252.7 MeV: Corrections

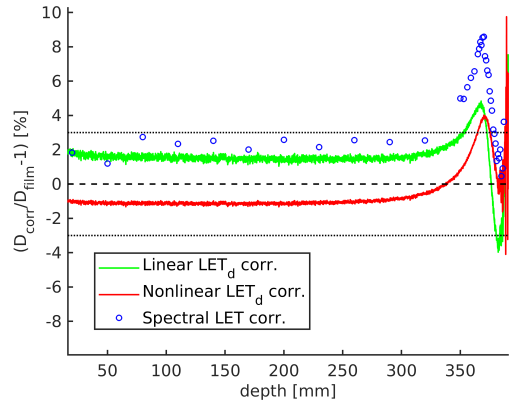

(f) 252.7 MeV: Residuals

Figure 4.26: The plots (a), (c) and (e) show detail views of the simulated depth dose curves of the single energy beams, including the film measurements and their associated fits over depth, and the different corrections applied to the MC dose to simulate the film measurements. The deviations of the corrections to the film fit are plotted on the right side.

The different film corrections, calculated using data only stemming from the single energy beams as described in section 3.5.2, applied to the MC dose, are shown in figure 4.27. Concerning the 62.4 MeV beam, the nonlinear LET_d correction agrees within 3% with the film fit calculated in section 4.4.1 up to the Bragg peak (29.5 mm), around which the deviation reaches 6%. For the 148.2 MeV beam the deviation of the same correction from the smoothed film dose remains below 3% over both plateau and peak. In the case of the 252.7 MeV beam the deviations range from roughly 1% in the plateau to 4% near the Bragg peak. The maximum deviations the linear LET_d correction exhibits are slightly larger for each of the beams, reaching roughly 6% (62.4 MeV), 4% (148.2 MeV) and 5% (252.7 MeV). While comparable to either of the LET_d corrections for the beams of smaller energy, the spectral LET correction shows a larger deviation between 5% and 9% from the film dose around the Bragg peak for the 252.7 MeV beam. The correction based on the discrete weights yields deviations almost identical to, or smaller than the spectral LET correction, reaching up to 3%, 3.5% and 7% for the 62.4, 148.2 and 252.7 MeV beam, respectively. For high dose gradients, all corrections exhibit large deviations ($> 10\%$) from the film dose. Hence the corrections are only compared up to R80 for the single energy beams. As shown in table 4.2, these ranges are approximately 29.9, 150.0 and 380.0 mm, from low to high inital beam energy, respectively.

Figure 4.27 shows the film corrections obtained from the monoenergetic beam data applied to the validation SOBPs. Up to depths of approximately 34.5 mm the nonlinear LET_d correction exhibits deviations up to 6% ($b1$), 3% ($b2$) and 2% ($b3$), compared to those of the linear correction, ranging up to 8% ($b1$), 6% ($b2$) and 2% ($b3$). Between depths of 31.0 and 34.5 mm, the split LET_d, i.e. the nonlinear LET_d correction applied to each of the single energy beams comprising an SOBP, respectively, and spectral LET correction yield similar residuals of 4-8% ($b1$), 2-6% ($b2$) and 2-4% ($b3$). Also for the validation SOBPs the discrete correction results in slightly smaller deviations over the whole investigated range, reaching up to 6%, 4.5% and 3% for $b1$, $b2$ and $b3$, respectively. Above 34.5 mm the deviations become large for all corrections due to the high dose gradient.

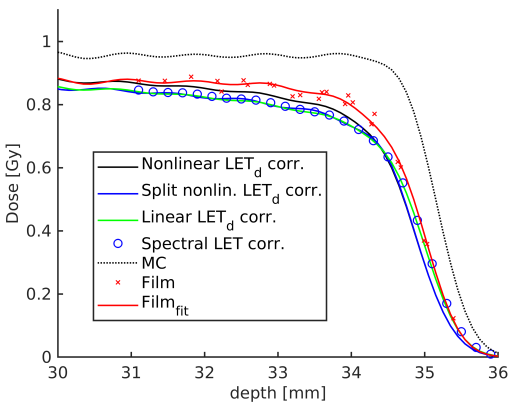

(a) b1 Corrections

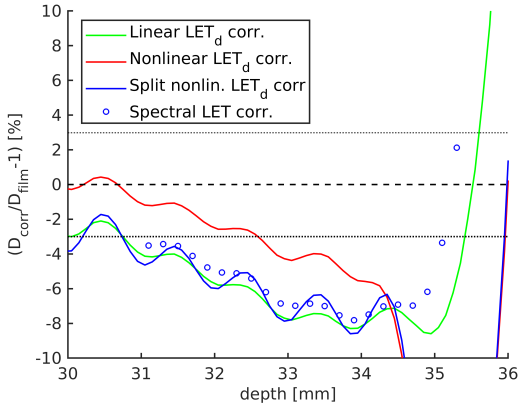

(b) b1: Residuals

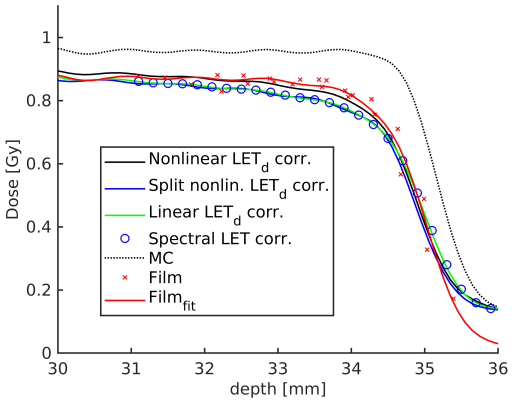

(c) b2: Corrections

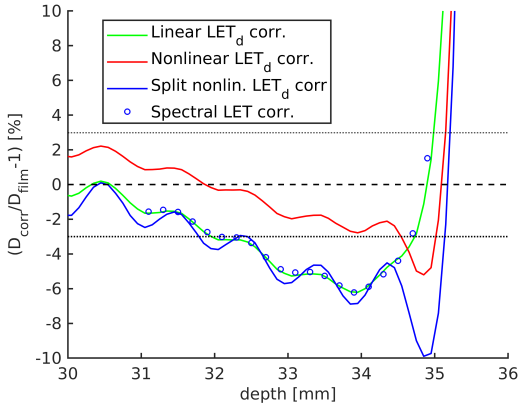

(d) b2: Residuals

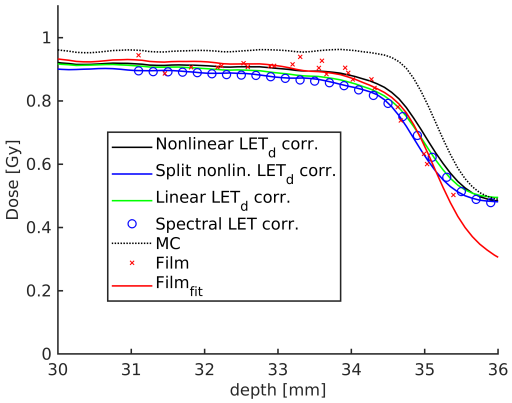

(e) b3: Corrections

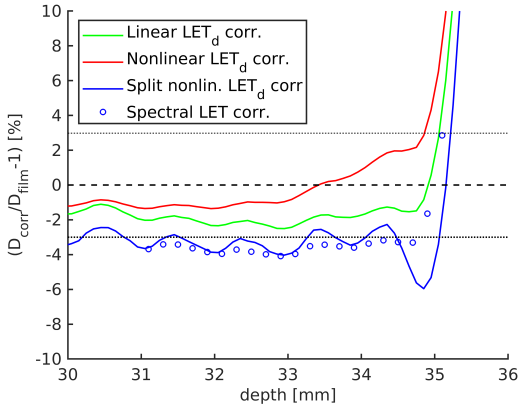

(f) b3: Residuals

Figure 4.27: Left column: MC simulated depth dose, film measurements with associated fits over depth, and corrections applied to MC dose for each of the SOBPs. Right column: Deviations between the corrections and the film fits.

4.5.3 Corrections calculated from SOBPs

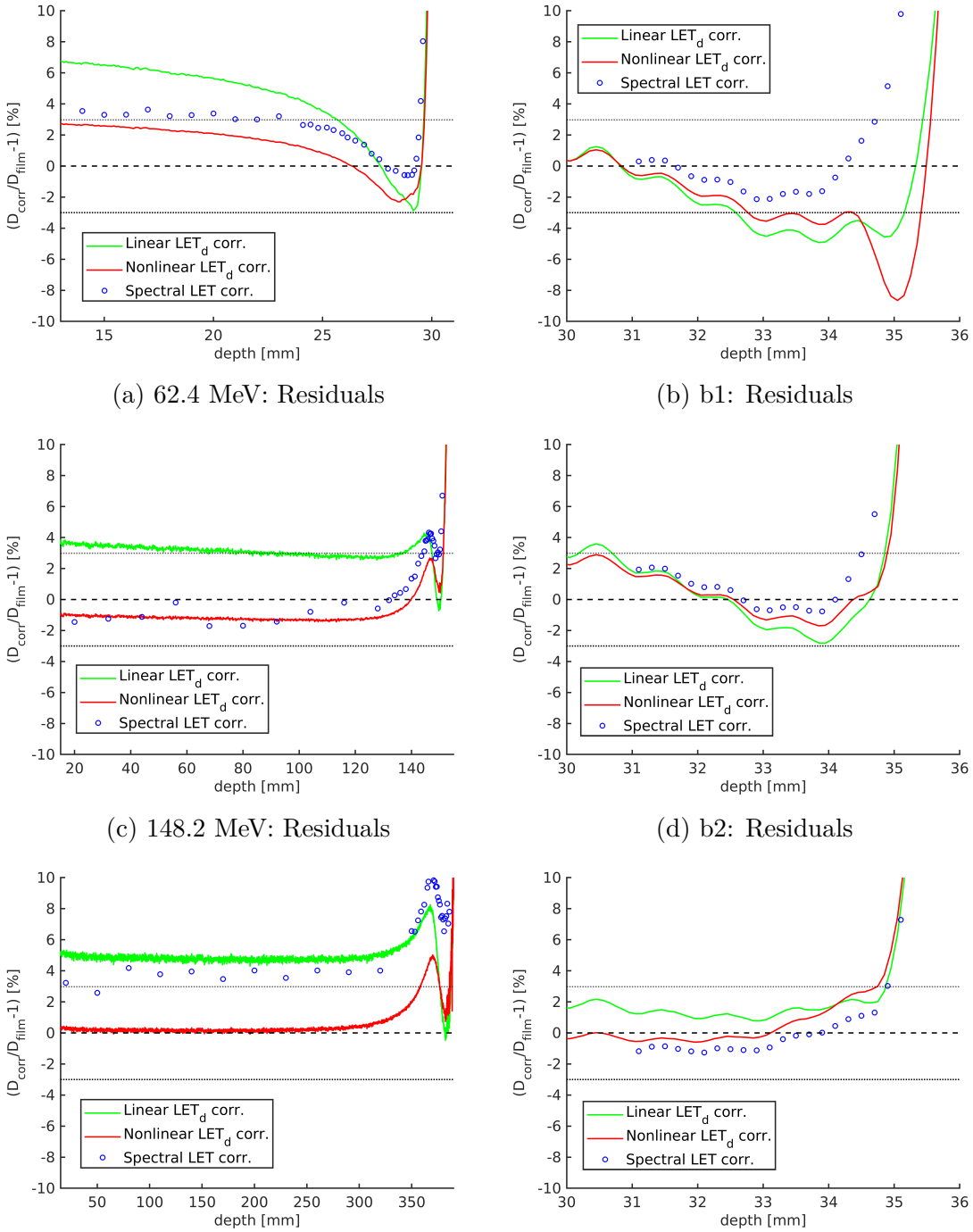

(a) 62.4 MeV: Residuals

(b) b1: Residuals

(c) 148.2 MeV: Residuals

(d) b2: Residuals

(e) 252.7 MeV: Residuals

(f) b3: Residuals

Figure 4.28: Deviations between the corrections based on SOBP measurements and the film fits. The left column shows the case for the corrections applied to the monoenergetic beams; on the right side the case for the SOBPs is shown.

Figure 4.28 (a), (c) and (e) show the film corrections, calculated from the SOBPs, validated against the single energy beams. The deviations between the nonlinear

LET_d corrected MC dose and the smoothed film dose are below 3% for the 62.4 MeV and 148.2 MeV beams, and below 5% for the 252.7 MeV beam, up to R80. The linear LET_d correction shows deviations of up to 7% (62.4 MeV), 4% (148.2 MeV) and 8% (252.7 MeV). The spectral LET correction agrees within 4% with the smoothed film dose of the 62.4 MeV and 148.2 MeV beam, while reaching deviations of 10% around the Bragg peak of the 252.7 MeV beam.

Film corrections, calculated from the SOBPs as described in section 3.5.2 and applied to the MC dose, are shown in the plots in the right column of figure 4.28. Up to 34.5 mm depth the nonlinear LET_d corrected dose agrees within 4% ($b1$) and 3% ($b2$ and $b3$) with the smoothed film dose. The linear LET_d correction yields deviations of 5% ($b1$), 4% ($b2$) and 2% ($b3$). For the same range in depth, the spectral LET corrected dose agrees within 2% with the film dose for all three SOBPs.

The discrete spectral correction yields poor results when validated against the single energy beams. While the correction around the Bragg peak is comparable to the other methods, deviations between corrected MC and measured film dose in the plateau reach values between 50% and almost 100%. Hence, the discrete corrections are not added to the plots for visibility.

Chapter 5

Discussion

Due to the relatively high measurement uncertainty associated with the EBT3 film dose measurements, initial attempts at improving the robustness of the measurements were made by comparing different calibration functions and readout methods. The results showed no large benefit of any calibration function over the investigated dose range, while the bimolecular model showed marginally better results and was hence used throughout this work. Neither was using multiple channels benefitial compared to the use of just one channel for the films used within this work. However, especially regarding the triple channel readout, it should be noted that the films used here were past their use-by date. As mentioned by Micke et al. [2011], the calibration curves of the individual channels are required to have sufficiently different gradients in order for the triple channel readout method to work well. The gradients change over time, most probably resulting in the poor results for the triple channel readout method for the films in this case, i.e., the dose was consistently corrected toward a lower dose, the magnitude of the correction limited by the optimization constraints.

This variation with time lends an argument to criticism of the use of calibrations not performed directly during the course of the measurement session and handled under approximately identical conditions (coined 'alien calibrations' throughout this work). Over the dose range investigated, different calibrations deviated up to 10% between each other for the red channel, as shown in section 4.1.3. Since it was observed that these deviations were smaller for the green channel, it was the choice of channel for all film doses calculated with an alien calibration. The thusly reduced systematic error was compensated though, by the increased statistical uncertainty associated with the green channel compared to the red one.

For both the single energy beams and the SOBPs the statistical uncertainy of the films is higher at points with steep dose gradients. A feasible explanation for this is that the films were slightly tilted in the holder. The fact that this statistical

uncertainty and the dose uncertainty induced by the positioning uncertainty are similar lends reassurance to the assumption of a positioning uncertainty of 0.1 mm within the holder. In a more conservative uncertainty estimation one may associate an even higher uncertainty with a possible systematic mispositioning of the entire holder in addition to the tilt within the holder.

Aside from points with steep dose gradients, the standard deviation of the netOD in the analyzed ROI does not show a dependence on the average netOD (or dose). Whether this noise stems from the quality of the EBT3 films, the homogeneity of the irradiated beams, the scanner or is a result of the film handling, remains unclear. The median values for the standard deviation of the netOD, i.e., neglecting points with steep dose gradient, were around 4% for red channel and 7% for the green one. In comparison, values between 3.5% and 10% were reported by Reinhardt et al. [2015].

In terms of dose, the noise was large compared to absolute measured dose at low doses, leading to large relative uncertainties of over 10% at 0.5 Gy in the plateau of the single energy beams, or roughly 7% at 1 Gy in the SOBPs. Higher accuracy may potentially be achieveable when irradiating higher doses (see for example Kirby et al. [2010]). There may be a trade-off between a higher signal to noise ratio and the dose uncertainty becoming larger due to the shape of the calibration curve closer to saturation.

The EBT3 film dose measurements displayed an under-response around the Bragg peak for the single energy beams, and the modulated peak for the SOBPs. For proton energies between 62.4 and 252.7 MeV, the under-response at the Bragg peak was found to range roughly between 10% and 30%, increasing to values between 15% and 70% at R50. For the SOBPs, comprising protons of the same energy range, the under-response increased from 5% to up to 30% over the modulated peak. Similar values have been reported previously, for example by Fiorini et al. [2014] measuring a 30% under-response at distal edge of a low energy SOBP.

The different trend for RE over residual range with varying initial beam energy was emphasized in figures 4.19 and 4.20, which were associated with the differences in the energy distribution of the beams. This outcome contradicts the results from Zhao and Das [2010], who modeled the RE as a function of residual range, thereby implicitly assuming the energy distribution to be roughly equal for different initial beam energies.

Investigation of the dose contribution of different particles and their associated LET_d showed that secondary protons deliver a non-negligible portion of the dose, reaching up to approximately 15%, while exhibiting larger LET_d values than the primaries. Thus, all protons, contributing over 98% of the dose, must be taken into account when modeling the RE as a function of beam quality.

While the LET of heavy particles is about an order of magnitude higher than for protons, they deliver a low dose contribution ($< 2\%$), deeming them negligible regarding the measurements and associated under-response. On the other hand it is instructive to examine LET_d^{all} of all particles, since it's behaviour differs substantially from the LET_d^{prot}, due to the inclusion of high LET particles. Considering the LET_d a generally robust model for the film under-response, any addition of otherwise negligible particles should not diminish the results. This is not the case, however, as demonstrated in figure 4.23, highlighting the limitations of the LET_d concept to just the average over protons.

In order to identify whether the dose or fluence averaging approach is valid, the SOBPs were created with differing LET distributions: Compared to $b1$, where both dose and fluence are made up of protons with the highest LET possible (lowest energy beams), 50% of the fluence was replaced with lowest LET protons (highest energy beam) for $b2$, and 50% of the dose was replaced with lowest LET protons for $b3$. While the dose averaged LET succesfully describes the under-response for all these cases, the RE cannot be described as a function of fluence averaged LET, as shown in figure 4.22. It follows that the fluence averaging concept is limited to unimodal LET distributions, and cannot succesfully be applied to more complex fields.

The LET_d^{prot} was shown to describe the under response of the films well for both monoenergetic beams and the SOBPs. A nonlinear model, a parametrized arcus tangens, provided a good fit to both data sets. A linear fit yielded parameters similar to those derived by Anderson et al. [2019], who concluded a relationship of $RE = (1.02 \pm 0.01) - (0.0251 \pm 0.0010) \times LET_d$, albeit only up to 10 keV/µm. The linear fits given in this work deviate maximally by 2.5% and 5.5%, calculated from the monoenergetic beam and SOBP data, respectively. However, this value becomes larger (roughly 7%) when fitting the linear function to all RE-values up to 10 keV/µm.

The RE was parametrized over depth for all measured beams using sigmoidal fits, simultaneously smoothing the RE and creating additional virtual data points for further analysis. The linear and nonlinear models of RE over LET_d were calculated using the results from the monoenergetic beams, and validated against the SOBPs. Comparison of these correction models with the RE fit over depth showed that the nonlinear approach produced smaller deviations up to 6%, whereas the linear function deviated up to 8%. Creating the fits based on the RE from the SOBPs and validating against the monoenergetic beams, further confirms the advantage of the nonlinear approach. This is put in perspective when taking into consideration the dose uncertainties of the film measurememnts, which were on average roughly 8.5%.

It thus follows that either correction is sufficient.

While the LET spectra of the monoenergetic beams are similar (unimodal), the spectra of the SOBPs varied substantially (partly non-unimodal) while resulting in the same dose averaged LET, as shown in figure 4.12. This prompted the application of the (nonlinear) LET_d correction to each individual beam comprising a SOBP, with the expectation of delivering more exact results. However, this split LET_d correction yielded larger deviations than all other tested corrections. The reason for this is presumably the large uncertainty at high LET_d (>10 keV/µm). While this influences the 'simple' corrections only at the dose fall-off, the split correction applies the resulting errors over the entire modulated peak, highlighting the importance of measurement and simulation accuracy.

The aim to include all simulated particles served as incentive to deviate from average LET concepts and investigate the entire LET spectrum. Taking the stark effects of the measurement inaccuracy to the split LET_d correction into consideration, optimisation of a weighting function over the LET spectrum was performed using only measurement points for which the accuracy of the film measurements, as well as the deviation between MC and IC were within 5%. Optimization of discrete weights over the LET spectrum was susceptible to the constraints and different training data used, though yielded a rough idea of the dependence on LET. In addition, a weighting function over LET was chosen roughly based on the discrete weights.

The parameters of this spectral weighting function were optimized using one set of data, and the resulting spectral correction validated against a different dataset. Choosing the SOBPs as the generating dataset lead to a more robust correction method. This is little surprising, considering the simulated SOBP spectra of $b2$ and $b3$ at all depths contain entries over the entire spectrum due to highest and lowest energy contribution, while for the single energy beams the high LET contribution is weighted heavier by default (see figure 4.11). The spectral correction yielded deviations below 3% over the modulated peak of the SOBPs, and within 4% up to R50 for the two lower monoenergetic beams. Only the 252.7 MeV beam was not described well, with the correction deviating up to 10% from the measured doses.

In comparison with the nonlinear dose averaged LET correction, the spectral approach shows a larger dependence on the training data used. For measurement points at depths of ample accuracy, i.e. within R50 and 34.5 mm for the monoenergetic beams and SOBPs, respectively, the nonlinear LET_d correction showed comparable to smaller deviations compared to the spectral correction. Thus, describing the RE of films as a nonlinear function of LET_d^{prot} when irradiated by proton beams yields better results compared to the other methods examined here, while being more versatile regarding the training data.

A possible dependence of the film effectiveness on the dose, in addition to the beam quality, as shown in Resch et al. [2019] (unpublished work), was not taken into account in this work. At constant LET_d the RE was shown to increase systematically with the dose, the effects being larger for higher doses, yielding up to to 12% increase in RE for 10 Gy compared to 0.5 Gy for an LET_d below 10 keV/µm. However, for the dose range of approximately 0 to 2 Gy examined in this work, the film response is expected to vary below 4% with the dose. Hence, any dose effect was out of scope.

Code of practice for dosimetry proposes a correction to be given with respect to the beam quality of calibration, Q_0, most commonly ^{60}Co gamma radiation. All corrections given in this work are implicitly given with respect to the calibration beam quality of a 179.2 MeV proton beam at 20 mm depth in water. That this Q_0 does not lead to a film quenching was not investigated within this work. However, other studies have shown that differences in film response between ^{60}Co radiation and proton beams in the clinically relevant energy range at shallow depths (up to 20 mm), are insignificantly small (Martišíková and Jäkel [2010b],Reinhardt et al. [2015]). Thus, it can be assumed that the 179.2 MeV calibration has negligible effect on the film quenching.

Assuming that the film quenching is solely dependent on LET, the corrections presented here are theoretically also applicable directly to carbon (or other heavy) ion beams. On the other hand, different particles with same LET may have different effects as is the case with RBE (Furusawa et al. [2000]). Investigations concerning EBT3 films and heavier ion beams are limited compared to protons. Castriconi et al. [2016] reported a RE of roughly 80% for EBT3 measurements of a 398.9 MeV/u carbon ion beam in water at 20 mm depth, corresponding to reference conditions in this work. The LET is given as 10 keV/µm, though the acquisition of this value is ambiguous and it is unclear whether this is a fluence or dose averaged quantity. Notwithstanding, such a result would be in good agreement with the results presented for protons within this work. A direct comparison of EBT3 film results for protons and other ions at same LET_d would be of interest in the future.

Dose measurements with films in combination with energy independent detectors would allow experimental determination of the beam quality, which in turn is used as an approximation of the relative biological effectiveness (RBE) of radiation (ICRP [2007]). Since the relationship between RBE and LET is not consistent for all particles and energy spectra, a better understanding of the beam quality effects on relatively simple films could lead to improvement of models for biological effectiveness and effective dose in general.

Chapter 6

Conclusion

In the scope of this thesis EBT3 film response was measured at different depths in three monoenergetic beams covering the clinically relevant energy range, and three SOBPs with different composition of high and low energy protons. An underresponse of up to 30% in the Bragg peak and modulated peak of the SOBPs was observed.

The beam quality and dose contribution from different particles were inferred from MC simulations for all irradiated beams. While secondary heavy particles contributed negligibly to the dose, this was not the case for secondary protons. Hence, both primary and secondary protons must be taken into account when describing the beam quality.

The relative effectiveness of the films was found to be a nonlinear function of dose averaged LET of the protons. This relationship was shown to become invalid when averaging over all particles, due the high LET of heavy secondaries. A functional dependence of RE on fluence averaged LET was proven to be false for SOBPs with non-unimodal distributions of dose over LET. It was hence concluded that corrections based on fluence averaging are conceptually limited.

Based on the relationship between RE and dose averaged LET and the LET spectrum, film quenching correction approaches were derived and compared using the single energy beam measurements as training data and validating against the SOBPs (and vice versa). The nonlinear LET_d correction was found to be the most robust and exact method, showing smaller or comparable deviations from the film dose compared to the other tested corrections, deviating maximally by 6% up until steep dose gradients, i.e., within the measurement accuracy. A parametrized arcus tangens was used in this work only since it provided the best fit, though yielding no insight into the mechanism underlying the film quenching.

Corrections applied to the entire LET spectrum had no benefit compared to the nonlinear LET_d correction, while exhibiting a strong dependence on the training

data used. Training data sets with the dose distributed over the whole LET spectrum were concluded to achieve more robust results. Derivation of a model based on theories behind film quenching, e.g. recombination or local saturation of polymerization, is proposed regarding the spectral correction for future investigations.

In addition, similar measurements as performed in this work but using ion beams could lead to better understanding of the possible dependence of film quenching on particle type.

A precise film correction was limited by the measurement uncertainty. Investigations of different film readout approaches showed that the most accurate film measurements are achieved by using the red channel only, though the green channel was found to be temporarily more reliable. No benefit of using multiple channels was found for the dose range examined here. The use of a correct calibration, i.e., performed on the day of a measurement, proved a more important factor. The large film to film variations of up to 10% did not allow a distinction between a 3rd and 1st order polynomial correction. In order to describe the RE correctly at steep dose gradients and derive a more reliable correction, film dosimetry needs to be improved in terms of accuracy and precision.

Abbreviations

SOBP	Spread-out Bragg Peak
IMT	Intensity modulated therapy
IC	Ionisation chamber
TLD	Thermoluminescent detector
LET	Linear energy transfer
EBT	External Beam Therapy
LET_t	Fluence (or track) averaged linear energy transfer
LET_d	Dose averaged linear energy transfer
CSDA	Continuous-slowing-down approximation
WET	Water equivalent thickness
OSLD	Optically stimulated luminescent detector
LiPCDA	Lithium-10,12-pentacosadiynoate
OD	Optical density
MC	Monte Carlo
PB	Pencil Beam
ROI	Region of interest
RE	Relative effectiveness
RBE	Relative biological effectiveness

Bibliography

Sea Agostinelli, John Allison, K al Amako, John Apostolakis, H Araujo, P Arce, M Asai, D Axen, S Banerjee, G 2 Barrand, et al. Geant4—a simulation toolkit. *Nucl. Instrum. Methods Phys. Res. Section A: Accelerators, Spectrometers, Detectors and Associated Equipment*, 506(3):250 – 303, 2003. ISSN 0168-9002.

Steven P Ahlen. Theoretical and experimental aspects of the energy loss of relativistic heavily ionizing particles. *Rev. Mod. Phys*, 52(1):121, 1980.

Sarah E Anderson, Michael P Grams, H Wan Chan Tseung, Keith M Furutani, and Chris J Beltran. A linear relationship for the LET-dependence of gafchromic EBT3 film in spot-scanning proton therapy. *Phys. Med. Biol.*, 64(5):055015, 2019.

G Battistoni, I Mattei, and S Muraro. Nuclear physics and particle therapy. *Adv. Phys: X*, 1(4):661–86, 2016.

M. J. Berger, M. Inokuti, H. H. Andersen, H. Bichsel, D. Powers, S . M. Seltzer, D . Thwaites, and D. E. Watt. ICRU Report 49: Stopping Powers and Ranges for Protons and Alpha Particles. *Journal of the International Commission on Radiation Units and Measurements*, os25(2):NP, 1993.

H Bethe. Zur Theorie des Durchgangs schneller Korpuskularstrahlen durch Materie. *Ann. Phys.*, 5:324–400, 1930.

F Bloch. Zur Bremsung rasch bewegter Teilchen beim Durchgang durch Materie. *Ann. Phys.*, 16:185–320, 1933.

Martin J Butson, KN Peter, Tsang Cheung, and Peter Metcalfe. Radiochromic film for medical radiation dosimetry. *Mater. Sci. Eng. R Rep*, 41(3-5):61–120, 2003.

C Candler. Photographic characteristic of a monolayer. *JOSA*, 52(3):300–12, 1962.

Roberta Castriconi, Mario Ciocca, Alfredo Mirandola, Carla Sini, Sara Broggi, Marco Schwarz, Francesco Fracchiolla, Mária Martišíková, Giulia Aricò, Giovanni Mettivier, et al. Dose–response of EBT3 radiochromic films to proton and carbon ion clinical beams. *Phys. Med. Biol.*, 62(2):377, 2016.

MB Chadwick, M Herman, P Obložinskỳ, Michael E Dunn, Y Danon, AC Kahler, Donald L Smith, B Pritychenko, Goran Arbanas, R Arcilla, et al. ENDF/B-VII. 1 nuclear data for science and technology: cross sections, covariances, fission product yields and decay data. *Nucl. Data Sheets*, 112(12):2887–996, 2011.

F Del Moral, JA Vázquez, JJ Ferrero, P Willisch, RD Ramirez, A Teijeiro, A López Medina, B Andrade, J Vázquez, F Salvador, et al. From the limits of the classical model of sensitometric curves to a realistic model based on the percolation theory for GafChromic™ EBT films. *Med. Phys.*, 36(9Part1):4015–26, 2009.

Alessio Elia. *Gate as a Geant4-based Monte-Carlo platform to support medical commissioning and Treatment Planning System verification in scanned ion beam therapy (Characterization of the GATE Monte Carlo platform for nonisocentric treatments and patient specific treatment plan verification at MedAustron)*. PhD thesis, Université de Lyon, 2019.

F Fiorini, D Kirby, J Thompson, S Green, DJ Parker, B Jones, and MA Hill. Under-response correction for EBT3 films in the presence of proton spread out Bragg peaks. *Physica Medica*, 30(4):454–61, 2014.

Y Furusawa, k Fukutsu, M Aoki, H Itsukaichi, K Eguchi-Kasai, H Ohara, F Yatagai, T Kanai, and K Ando. Inactivation of aerobic and hypoxic cells from three different cell lines by accelerated 3He-, 12C- and 20Ne-ion beams. *Radiat. Res.*, 154 (5):485–96, 2000.

C Grassberger and H Paganetti. Elevated LET components in clinical proton beams. *Phys. Med. Biol.*, 56(20):6677–91, 2011.

V Grilj and DJ Brenner. LET dependent response of GafChromic films investigated with MeV ion beams. *Phys. Med. Biol.*, 63(24):245021, 2018.

Helen Gustavsson, Sven Å J Bäck, Joakim Medin, Erik Grusell, and Lars E Olsson. Linear energy transfer dependence of a normoxic polymer gel dosimeter investigated using proton beam absorbed dose measurements. *Phys. Med. Biol.*, 49(17): 3847, 2004.

Naoki Hayashi, Yoichi Watanabe, Ryan Malmin, and Hideki Kato. Evaluation of triple channel correction acquisition method for radiochromic film dosimetry. *J. Radiat. Res. (Tokyo)*, 53(6):930–35, 2012.

TRS IAEA. 398. Absorbed dose determination in external beam radiotherapy: An International Code of Practice for Dosimetry based on standards of absorbed dose to water. *Vienna International Atomic Energy Agency*, 2000.

2007 ICRP. The 2007 Recommendations of the International Commission on Radiological Protection: ICRP Publication 103. *Ann. ICRP*, 37:1–332, 2007.

Anton V Ivantchenko, Vladimir N Ivanchenko, Jose-Manuel Quesada Molina, and Sebastien L Incerti. Geant4 hadronic physics for space radiation environment. *Int. J. Radiat. Biol.*, 88(1-2):171–75, 2012.

Andrew Jirasek and Cheryl Duzenli. Relative effectiveness of polyacrylamide gel dosimeters applied to proton beams: Fourier transform Raman observations and track structure calculations. *Med. Phys.*, 29(4):569–77, 2002.

Suphalak Khachonkham, Ralf Dreindl, Gerd Heilemann, Wolfgang Lechner, Hermann Fuchs, Hugo Palmans, Dietmar Georg, and Peter Kuess. Characteristic of EBT-XD and EBT3 radiochromic film dosimetry for photon and proton beams. *Phys. Med. Biol.*, 63(6):065007, 2018.

Daniel Kirby, Stuart Green, Hugo Palmans, Richard Hugtenburg, Cecile Wojnecki, and David Parker. LET dependence of GafChromic films and an ion chamber in low-energy proton dosimetry. *Phys. Med. Biol.*, 55(2):417–33, 2010.

Aafke Christine Kraan. Range Verification Methods in Particle Therapy: Underlying Physics and Monte Carlo Modeling. *Front. Oncol.*, 5:150, 2015.

Gerhard Kraft. Tumor therapy with heavy charged particles. *Prog. Part. Nucl. Phys*, 45:S473–S544, 2000.

Tomasz Kubiak. Beam delivery systems in hadron therapy for cancer treatment. *PiJ*, 1:67–73, 2014.

Elsa Y León-Marroquín, José M Lárraga-Gutiérrez, J Alfredo Herrera-González, Miguel A Camacho-López, Jose E Villarreal Barajas, and Olivia A García-Garduño. Investigation of EBT 3 radiochromic film's response to humidity. *J. Appl. Clin. Med. Phys.*, 19(3):283–90, 2018.

D Lewis. Radiochromic film. *Wayne, NJ: International Specialty Products*, 2010.

David F Lewis and Maria F Chan. Technical Note: On GAFChromic EBT-XD film and the lateral response artifact. *Med. Phys.*, 43(2):643–49, 2016.

Bart D Lynch, Jakub Kozelka, Manisha K Ranade, Jonathan G Li, William E Simon, and James F Dempsey. Important considerations for radiochromic film dosimetry with flatbed CCD scanners and EBT film. *Med. Phys.*, 33(12):4551–56, 2006.

Mária Martišíková and Oliver Jäkel. Study of Gafchromic® EBT film response over a large dose range. *Phys. Med. Biol.*, 55(10):N281, 2010a.

Mária Martišíková and Oliver Jäkel. Dosimetric properties of Gafchromic® EBT films in monoenergetic medical ion beams. *Phys. Med. Biol.*, 55(13):3741, 2010b.

Andre Micke, David F Lewis, and Xiang Yu. Multichannel Film Dosimetry with Nonuniformity Correction. *Med. Phys.*, 38(5):2523–34, 5 2011.

Wayne D Newhauser and Rui Zhang. The physics of proton therapy. *Phys. Med. Biol.*, 60(8):R155–R209, 2015.

NIST. Stopping-Power & Range Tables for Electrons, Protons, and Helium Ions, 2017. URL `www.nist.gov/pml/stopping-power-range-tables-electrons-protons-and-helium-ions`.

LEEN Paelinck, Wilfried De Neve, and Carlos De Wagter. Precautions and strategies in using a commercial flatbed scanner for radiochromic film dosimetry. *Phys. Med. Biol.*, 52(1):231, 2006.

H Paganetti. Nuclear interactions in proton therapy: dose and relative biological effect distributions originating from primary and secondary particles. *Phys. Med. Biol.*, 47(5):747, 2002.

Lech Papiez and Jerry J Battista. Radiance and particle fluence. *Phys. Med. Biol.*, 39(6):1053, 1994.

L A Perles, D Mirkovic, A Anand, U Titt, and R Mohan. LET dependence of the response of EBT2 films in proton dosimetry modeled as a bimolecular chemical reaction. *Phys. Med. Biol.*, 58(23):8477, 2013.

S Reinhardt, M Hillbrand, JJ Wilkens, and W Assmann. Comparison of Gafchromic EBT2 and EBT3 films for clinical photon and proton beams. *Med. Phys.*, 39(8): 5257–62, 2012.

S Reinhardt, M Würl, C Greubel, N Humble, JJ Wilkens, M Hillbrand, A Mairani, W Assmann, and K Parodi. Investigation of EBT2 and EBT3 films for proton dosimetry in the 4–20 MeV energy range. *Radiat. Environ. Biophys.*, 54(1):71–79, 2015.

Andreas F Resch, Paul D Heyes, Hermann Fuchs, Niels Bassler, Dietmar Georg, and Hugo Palmans. Comparing different averaging concepts to correct for the beam quality effect of Gafchromic EBT3 films in proton therapy. 2019.

M. Rosetti R.F. Laitano and M. Frisoni. Effects of nuclear interactions on energy and stopping power in proton beam dosimetry. *Nuclear Instruments and Methods in Physics Research Section A: Accelerators, Spectrometers, Detectors and Associated Equipment*, 376(3):466 – 476, 1996. ISSN 0168-9002.

Alexandra Rink, I Alex Vitkin, and David A Jaffray. Characterization and real-time optical measurements of the ionizing radiation dose response for a new radiochromic medium. *Med. Phys.*, 32(8):2510–16, 2005a.

Alexandra Rink, I Alex Vitkin, and David A Jaffray. Suitability of radiochromic medium for real-time optical measurements of ionizing radiation dose. *Med. Phys.*, 32(4):1140–55, 2005b.

Alexandra Rink, David F Lewis, Sangya Varma, I Alex Vitkin, and David A Jaffray. Temperature and hydration effects on absorbance spectra and radiation sensitivity of a radiochromic medium. *Med. Phys.*, 35(10):4545–55, 2008.

David Sarrut, Manuel Bardiès, Nicolas Boussion, Nicolas Freud, Sébastien Jan, Jean-Michel Létang, George Loudos, Lydia Maigne, Sara Marcatili, Thibault Mauxion, et al. A review of the use and potential of the GATE Monte Carlo simulation code for radiation therapy and dosimetry applications. *Med. Phys.*, 41(6Part1): 064301, 2014.

Dieter Schardt, Thilo Elsässer, and Daniela Schulz-Ertner. Heavy-ion tumor therapy: Physical and radiobiological benefits. *Rev. Mod. Phys*, 82(1):383, 2010.

S.M. Seltzer, D.T. Bartlett, D.T. Burns, H.-G Menzel, H.G. Paretzke, and A Wambersie. ICRU Report 85: Fundamental Units and Quantities for ionizing radiation (revised). *Journal of the International Commission on Radiation Units and Measurements*, 11(1):1–33, 2011.

X. Tian, K. Liu, Y. Hou, J. Cheng, and J Zhang. The evolution of proton beam therapy: Current and future status (Review). *Molecular and Clinical Oncology*, 8 (1):15–21, 2018.

Yung-Su Tsai. Pair production and bremsstrahlung of charged leptons. *Rev. Mod. Phys.*, 46:815–51, Oct 1974.

G Wegner. Topochemical polymerization of monomers with conjugated triple bonds. *Macromol. Chem. Phys.*, 154(1):35–48, 1972.

Gerhard Wegner. Solid-state polymerization mechanisms. In *Photochemical Processes in Polymer Chemistry–2*, pages 443–54. Elsevier, 1977.

Robert R. Wilson. Radiological Use of Fast Protons. *Radiology*, 47(5):487–91, 1946.

Li Zhao and Indra J Das. Gafchromic EBT film dosimetry in proton beams. *Phys. Med. Biol.*, 55(10):291, 2010.

Appendix A

Derivation of unbiased pooled variance

Let several subsets of data be combined to a pooled data set. The N individual values x_i are not known, however, of each subset the number of measurements n_k, the mean $\overline{x}_k$ and standard deviation σ_k are given. The overall mean μ may be easily inferred.

Starting point is the variance of all individual measurements, which is to be expressed in terms of the known data from the subsets. The variance may be re-written as

$$\begin{aligned}\sigma^2 &= \frac{1}{N-1}\sum_{i=1}^{N}(x_i-\mu)^2 \\ &= \frac{1}{N-1}\left[\sum_{i=1}^{N}(x_i^2) - 2\mu\sum_{i=1}^{N}(x_i^2) + \sum_{i=1}^{N}(\mu)\right] \\ &= \frac{1}{N-1}\left[\sum_{i=1}^{N}(x_i^2) - N\mu\right],\end{aligned} \tag{A.1}$$

which is known as the Steiner translation theorem.

The data is divided into K subsets of arbitrary size n_k, such that

$$\mu = \frac{1}{N}\sum_{i=1}^{N}(x_i) = \frac{1}{N}\sum_{k=1}^{K}(n_k\overline{x}_k). \tag{A.2}$$

Analogous to equation A.1, the variance of the subsets may be written as

$$\sigma_k^2 = \frac{1}{n_k-1}\left[\sum_{i=1}^{n_k}(x_i^2) - n_k\overline{x}_k^2\right] \tag{A.3}$$

or

$$\sum_{i=1}^{n_k}(x_i^2) = (n_k-1)\sigma_k^2 + n_k\overline{x}_k^2. \tag{A.4}$$

Thus the sum over all x_i^2 may be expressed in terms of subsets

$$\sum_{i=1}^{N} x_i^2 = \sum_{k=1}^{K} \sum_{j=1}^{n_k} x_j^2 = \sum_{k=1}^{K} \left[(n_k - 1)\sigma_k^2 + n_k \overline{x}_k^2 \right]. \tag{A.5}$$

Inserting this into the initial equation A.1 yields the unbiased pooled variance

$$\begin{aligned} \sigma^2 &= \frac{1}{N-1} \left[\sum_{k=1}^{K} (n_k - 1)\sigma_k^2 + \sum_{k=1}^{K} (n_k \overline{x}_k^2) - N\mu^2 \right] \\ &= \frac{1}{N-1} \sum_{k=1}^{K} \left[(n_k - 1)\sigma_k^2 + n_k (\overline{x}_k - \mu)^2 \right]. \end{aligned} \tag{A.6}$$

List of Figures

List of Tables